

Mapping Firn Saturation over Greenland using NASA's Soil Moisture Active Passive Satellite

Julie Z. Miller, David G. Long, *Fellow, IEEE*, Christopher A. Shuman,
Riley Culberg, *Student Member, IEEE*, Molly Hardman, Mary J. Brodzik, *Member, IEEE*

Abstract—Mapping the spatial extent of recently identified englacial hydrological features (i.e., ice slabs and perennial firn aquifers) formed by meters-thick water-saturated firn layers over the percolation facies of the Greenland Ice Sheet using L-band microwave radiometry has recently been demonstrated. However, these initial maps are binary, and do not provide a parameter to estimate the spatial variability in the thickness and volumetric fraction of meltwater stored within the firn pore space. Here, we exploit enhanced-resolution vertical-polarization L-band brightness temperature (T_V^B) imagery (2015–2019) generated using observations collected over Greenland by NASA's Soil Moisture Active Passive (SMAP) satellite and a simple two-layer L-band brightness temperature model. We map water-saturated firn layers via a ‘firn saturation’ parameter, and interpret our results together with perennial firn aquifer and ice slab spatial extents, estimates of snow accumulation simulated via the Regional Atmospheric Climate Model (RACMOp2.3), and airborne radar surveys collected via NASA's Operation IceBridge (OIB) campaigns. We find that variable firn saturation parameter values are mapped in lower snow accumulation ice slab areas in western, northern, and northeastern Greenland, where firn is colder and water-saturated firn layers seasonally refreeze as solid-ice. Higher firn saturation parameter values are mapped in higher snow accumulation perennial firn aquifer areas in southeastern, southern, and northwestern Greenland, where firn is near the melting point, and meters-thick water-saturated firn layers exist. Our results have implications for identifying expansive englacial reservoirs that store significant volumes of meltwater in locations that are vulnerable to meltwater-induced hydrofracturing and accelerated outlet glacier flow year-round.

Index Terms—Greenland Ice Sheet, firn saturation, remote sensing, L-band microwave radiometry, Soil Moisture Active Passive (SMAP)

Manuscript received X X, 2021; revised X X, 2021; accepted X X, 2021. Date of publication X X, 2022; date of current version X X, 2022. This work is supported by the NASA SMAP Science Team (80NSSC20K1806) and by the NASA Cryospheric Science Program (80NSSC18K1055, 80NSSC21K0749). Riley Culberg is supported by a National Defense Science and Engineering Graduate Fellowship. (Corresponding author: Julie Z. Miller)

J. Z. Miller is with the Earth Science and Observation Center, Cooperative Institute for Research in Environmental Sciences, University of Colorado Boulder, Boulder, CO 80309 USA (e-mail: jzmiller.research@gmail.com).

D. G. Long is with Department of Electrical and Computer Engineering, Brigham Young University, Provo, UT 84602 USA (e-mail: long@ee.byu.edu).

C. A. Shuman is with the University of Maryland, Baltimore County at NASA's Goddard Space Flight Center, Greenbelt, MD 20771 USA (e-mail: cshuman@umbc.edu).

R. Culberg is with the Department of Electrical Engineering, Stanford University, Stanford, CA 94305 USA (e-mail: culberg@stanford.edu).

M. J. Brodzik and M. Hardman are with the National Snow and Ice Data Center, Cooperative Institute for Research in Environmental Sciences, University of Colorado Boulder, Boulder, CO 80309 USA (e-mail: brodzik@colorado.edu, molly.hardman@colorado.edu).

I. INTRODUCTION

Recently launched low-frequency (1.4 GHz) satellite microwave radiometry missions – such as NASA's Aquarius Mission [1], ESA's Soil Moisture Ocean Salinity Mission (SMOS) mission [2], and NASA's L-band Soil Moisture Active Passive (SMAP) mission [3] – enable mapping global sea surface salinity and terrestrial soil moisture from space. However, these missions also have potential for cryospheric applications over Earth's polar ice sheets as a result of large penetration depths that can probe as deep as the underlying bedrock [4], [5] or ocean. While higher-frequency (6–37 GHz) satellite microwave radiometry missions have been extensively used to map seasonal surface and near-surface meltwater to depths of a few meters over ice sheets since early in the satellite era e.g., [6], [7], [8], [9], low-frequency satellite microwave radiometry missions are capable of mapping seasonal surface and near-surface meltwater e.g., [10], [11], [12], [13], [14] as well as subsurface meltwater to depths of tens to hundreds of meters. This capability allows for mapping englacial hydrological features, such as ice slabs and perennial firn aquifers [15], [16], and subglacial hydrological features, such as large subglacial lakes [4], beneath the surface of the polar ice sheets.

The objective of this study is to further exploit enhanced-resolution vertical-polarization L-band brightness temperature (T_V^B) imagery (2015–2019) generated using observations collected over Greenland by the microwave radiometer on NASA's SMAP satellite [17] to map water-saturated firn layers from space. We calculate a ‘firn saturation’ parameter derived from a simple two-layer L-band brightness temperature model [16] using both conventionally processed SMAP T_V^B imagery generated by a ‘drop-in-the-bucket’ (GRD) algorithm, and enhanced-resolution SMAP T_V^B imagery generated by the radiometer form of the Scatterometer Image Reconstruction (rSIR) algorithm [17]. We then interpret the rSIR mapping of the firn saturation parameter together with ice slab and perennial firn aquifer spatial extents mapped using SMAP rSIR T_V^B imagery and an empirical algorithm [16], estimates of snow accumulation simulated via the Regional Atmospheric Climate Model (RACMOp2.3) [18], and airborne radar surveys collected via NASA's Operation IceBridge (OIB) campaigns [19].

The paper is organized as follows. A background on previous work is provided in Section II. A description of the methods used in this study is provided in Section III. Section IV provides an interpretation of our results. We conclude with a summary and discussion of future work in Section V.

II. MAPPING ENGLACIAL HYDROLOGICAL FEATURES

The percolation facies of the Greenland Ice Sheet are characterized by heterogeneous vertical and lateral percolation of seasonal meltwater into porous snow and firn layers at depth during the melting season [23], [20], [21], [22]. Depending on the local climate, subsurface meltwater may refreeze as embedded ice structures [23], [21], or may be stored within englacial reservoirs. During the freezing season, vertically-oriented ice pipes form when seasonal meltwater refreezes in percolation channels. Horizontally-oriented ice layers and ice lenses form when seasonal meltwater refreezes on semi-impermeable layers deeper within the firn. Shallow water-saturated firn layers often fully refreeze, forming either a network of embedded ice structures consisting of discontinuous ice layers and ice lenses sparsely connected via ice pipes (i.e., spatially coherent melt layers) [24], or dense, low-permeability, solid-ice layers (i.e., ice slabs) [25], [26]. Seasonal meltwater may also be stored intermittently on top of existing ice slabs or other impermeable layers [27], or at the physical limit of vertical meltwater percolation in firn [28], forming perched firn aquifers. In contrast, deep water-saturated firn layers may be perennially stored and can extend from near the ice sheet surface to the firn-ice transition [29], [30]. Such meters-thick water-saturated firn layers that exist year-round and are known as perennial firn aquifers [31], [32], [33].

The percolation facies boundaries are interannually variable and delineated by the dry snow facies and the wet snow facies as well as the low-elevation ($<\sim 1000$ m a.s.l.) ablation facies [23]. The dry snow facies are located in the high-elevation ($>\sim 2500$ m a.s.l.) interior and represent the upper boundary of the percolation facies, which is defined by the dry snow line. This region experiences negligible surface melting, and is characterized by snow and firn layers extending from the ice sheet surface to the firn-ice transition. The wet snow facies are located in the lower-elevations ($<\sim 1500$ m a.s.l.) and represent the lower boundary of the percolation facies. This region typically experiences extensive surface melting. The upper snow layer is completely saturated with seasonal meltwater that refreezes as a superimposed ice layer overlying deeper glacial ice.

Miller [15] first demonstrated the novel use of the L-band microwave radiometer on NASA's SMAP satellite for mapping perennial firn aquifers in the percolation facies of the Greenland Ice Sheet from space (Fig. 1). In that study, exponentially decreasing temporal L-band signatures observed in SMAP rSIR T_V^B time series were correlated with perennial firn aquifer detections [32] identified via airborne ice-penetrating radar surveys collected by NASA's OIB campaigns [19]. An empirical algorithm to map spatial extent was developed by fitting exponentially decreasing temporal L-band signatures to a set of sigmoidal curves derived from the continuous logistic model. The relationship between the radiometric, and therefore the physical, temperature of perennial firn aquifer areas, as compared to other percolation facies areas, forms the basis of the empirical algorithm. That study hypothesized that the dominant control on the exponential rate of decrease in temporal L-band signatures over perennial firn aquifer areas

is physical temperature versus depth. However, more recent work by Jezek [34] suggests the complex interplay between physical temperature, the volumetric fraction of meltwater stored within the water-saturated firn layers, latent heat, and volume scattering from embedded ice structures dominates depth-integrated L-band emission over perennial firn aquifer areas during the freezing season.

[Fig. 1 about here.]

Miller [16] adapted the empirical algorithm developed in [15] and demonstrated mapping ice slabs and perennial firn aquifers together as a continuous system over the percolation facies of the Greenland Ice Sheet from space (Fig. 1). The expanded relationship between the radiometric temperature of each of these englacial hydrological features forms the basis of the adapted empirical algorithm. Analyses of spatiotemporal differences in SMAP rSIR T_V^B imagery and temporal L-band signatures were used to derive a firn saturation parameter from a simple two-layer L-band brightness temperature model [9], [35]. The firn saturation parameter estimates the spatial variability in the thickness and volumetric fraction of meltwater stored within the firn pore space, and was integrated into the adapted empirical algorithm to map binary spatial extents. That study concluded that ice slabs and perennial firn aquifer areas represent distinct, but related, sub-facies within the broader percolation facies that can be defined by differences in snow accumulation, which influences the englacial hydrology and thermal characteristics of the firn at depth.

III. METHODS

A. Satellite L-band Microwave Radiometry

NASA's SMAP satellite was launched 31 January 2015 and flies at a 685 km altitude, 98.1° inclination, polar orbit [3]. Operating at an L-band (1.41 GHz) frequency, the microwave radiometer on the SMAP satellite is currently collecting brightness temperature (T^B) observations of the horizontal, vertical, and 3rd and 4th Stokes parameter polarizations over Greenland at a nominal incidence angle of 40° , and a total radiometric uncertainty of approximately 1.3 K [36]. The antenna spin rate is 14.6 rpm which, when coupled with the along-track motion of the satellite, produces a helical antenna scan pattern on the Earth's surface with an along-track spacing of approximately 31 km between antenna rotations.

Conventionally processed SMAP GRD T^B imagery generated using a drop-in-the-bucket algorithm provide low-noise levels, but also low spatial resolution. SMAP GRD T^B imagery is generated by averaging all satellite observations within a discrete time interval whose center locations fall within the bounds of a particular grid cell. The rSIR algorithm was developed to reconstruct conventionally processed SMAP GRD T^B imagery on a finer spatial resolution grid [17], [37]. It exploits the measurement response function (MRF) for each satellite observation, which is a smeared version of the helical antenna scan pattern. Using the overlapping MRFs, the rSIR algorithm reconstructs T^B from the spatially filtered, low-resolution sampling provided by the satellite observations. In effect, it generates an MRF-deconvolved T^B image.

Combining multiple satellite orbital passes within a discrete time interval increases the sampling density, which improves the accuracy and resolution of the reconstruction [17]. Finer spatial resolution SMAP rSIR T^B imagery generated using the rSIR algorithm have higher noise levels. Thus, the differing SMAP GRD and rSIR T^B imagery provide a tradeoff between effective resolution and noise [17], [37], [38], [39].

Conventionally processed SMAP GRD and reconstructed rSIR T^B imagery have been generated as part of the SMAP Radiometer Twice-Daily rSIR-Enhanced EASE-Grid 2.0 Brightness Temperatures, Version 1, Data Set [17]. The GRD and rSIR algorithms separately combine satellite orbital passes that occur between 8 a.m. and 4 p.m. local time-of-day over Greenland to generate imagery twice daily (i.e., morning and evening satellite orbital pass intervals, respectively). This minimizes fluctuations in the observed T^B at high latitudes due to changes in the physical temperature from local daily temperature cycling, and provides improved temporal resolution, permitting resolution of diurnal variations [37]. SMAP GRD and rSIR T^B imagery are projected on Northern Hemisphere Equal-Area Scalable Earth Grids (EASE-Grid 2.0) [40] at a 25 km and 3.125 km grid cell spacing, respectively. The effective resolution for each grid cell is dependent on the number of satellite observations used in the gridding algorithm, and is coarser than the grid cell spacing. While the effective resolution of conventionally processed SMAP GRD T^B imagery posted on a 25 km grid is approximately 30 km, the effective resolution of SMAP rSIR T^B imagery posted on a 3.125 km grid is approximately 18 km, an improvement of up to 60%. The tradeoff is up to 70% higher noise [17].

As previously noted, for this study we use both GRD and rSIR T_V^B imagery over Greenland. As compared to the horizontal-polarization channel, the vertical-polarization channel exhibits decreased sensitivity to changes in the volumetric fraction of meltwater, which is attributed to reflection coefficient differences between channels [15], [16]. The Greenland Ice Mapping Project (GIMP) Land Ice and Ocean Classification Mask, Version 1, Data Set [43] is projected on a Northern Hemisphere EASE-Grid 2.0 at a 25 km GRD and 3.125 km rSIR grid cell spacing, respectively. The derived ice mask includes the Greenland Ice Sheet and its peripheral ice caps. We construct annual ice-masked SMAP GRD and rSIR T_V^B image time series between 1 April 2015 and 31 March 2019 that alternate morning and evening satellite observations.

Our analysis of temporal L-band signatures over the percolation facies suggests that deeper firn layers are saturated with seasonal meltwater quickly (i.e., time scales of weeks) following melt onset, and remain water-saturated throughout the melting season. We postulate that firn saturation results in a superimposed signal – where the rapidly-varying signal induced by near-surface melting and refreezing that occurs as a result of daily temperature cycling is superimposed over the slowly-varying signal from deeper water saturated firn layers.

B. Two-Layer L-band Brightness Temperature Model

The firn saturation parameter [16] is derived from a two-layer L-band brightness temperature model [9], [35] that

assumes a base layer underlying a water-saturated firn layer with a given depth and volumetric fraction of meltwater. Each of the layers is uniform. The ice sheet is discretely layered to calculate emission at an oblique incidence angle (Eq. 1). Emission from the base layer is a function of both the macroscopic roughness and the dielectric properties. It occurs in conjunction with volume scattering at depth, and is locally dependent on englacial hydrological features, including embedded ice structures, spatially coherent melt layers, ice slabs, and perched and perennial firn aquifers. Buried supraglacial lakes may also influence base layer emission [16]. Reflectivity at depth (i.e., at the base layer-water-saturated firn layer interface), and at the ice sheet surface (i.e., at the water-saturated firn layer-air interface) is neglected. The contribution from each layer is individually calculated.

The two-layer brightness temperature model is represented analytically by

$$T_{V,max}^B = T (1 - e^{-\kappa_e d \sec \theta}) + T_{V,min}^B e^{-\kappa_e d \sec \theta}, \quad (1)$$

where $T_{V,min}^B$ is the minimum vertical-polarization brightness temperature emitted from the base layer. $T_{V,max}^B$ is the maximum vertical-polarization brightness temperature at the ice sheet surface, and represents emissions from the maximum volumetric fraction of meltwater stored within the water-saturated firn layer. T is the physical temperature of the water-saturated firn layer, θ is the transmission angle, κ_e is the extinction coefficient, and d is the depth.

We invert Eq. 1, and then solve for the firn saturation parameter (ξ)

$$\xi = -\ln \left(\frac{T_{V,max}^B - T}{T_{V,min}^B - T} \right) \cos \theta, \quad (2)$$

where $\xi = \kappa_e d$. $T_{V,max}^B$ asymptotically approaches the physical temperature of the water-saturated firn layer as the extinction coefficient and the depth of the water-saturated firn layer increases. For simplicity, we follow Jezek [4] and define the extinction coefficient as the sum of the Raleigh scattering coefficient (κ_s) and the absorption coefficient (κ_a). This assumes scattering from snow grains, which are small (millimeter scale) relative to the L-band wavelength (21 cm), and neglects Mie scattering from large (centimeter scale) embedded ice structures. However, for water-saturated firn, absorption dominates over scattering, and increases in the extinction coefficient are controlled by the volumetric fraction of meltwater (m_v) [42].

We calculate the firn saturation parameter from the SMAP GRD and rSIR T_V^B image time series. For each GRD and rSIR grid cell within the ice-masked spatial extent, we calculate $T_{V,min}^B$ and $T_{V,max}^B$ by smoothing T_V^B time series using a 14-observation (1-week) temporal averaging window, and then estimating the maximum and minimum values. We note that smoothing T_V^B time series may mask brief low-intensity surface melting events that occur in the high-elevation percolation facies, and slightly underestimate the mapped spatial extent [16]. $T_{V,min}^B$ is chosen prior to $T_{V,max}^B$ to avoid detecting changes in T_V^B values that may occur as a result of changes in ice sheet stratigraphy during or following the melting season (e.g., the formation of embedded ice structures, changes in

the depth or volumetric fraction of meltwater stored within the firn pore space of perennial or perched firn aquifers). We set the physical temperature of the water-saturated firn layer to $T=273.15$ K, and the transmission angle to $\theta=40^\circ$. We then calculate ξ . Following Miller [16], we set the firn saturation parameter threshold to $\xi_T = 0.1$, which corresponds to a uniform water-saturated firn layer with a depth of $d=1$ m, and a volumetric fraction of meltwater of $m_v=1\%$. If the calculated firn saturation parameter exceeds the firn saturation parameter threshold ($\xi > \xi_T$), the grid cell is mapped. The resulting total grid cell spatial extent represents the percolation facies.

We assume that thicker water-saturated firn layers with larger volumetric fractions of meltwater generate higher firn saturation parameter values. However, the observed thickness of the water-saturated firn layer is limited by the penetration depth. Miller [16] estimated theoretical L-band penetration depths for a uniform layer of water-saturated firn using the empirically-derived models for the complex dielectric constant described by Tiuri [41], which are calculated as a function of m_v . Theoretical L-band penetration depths calculated for a water-saturated firn layer range from between approximately 10 m for small volumetric fractions of meltwater ($m_v=1\%$), and 1 cm for large volumetric fractions of meltwater ($m_v=20\%$). Large volumetric fractions of meltwater stored within the firn pore space results in high reflectivity and attenuation at the water-saturated firn layer-air interface, and a radiometrically cold firn layer.

C. Empirical Algorithm

The empirical algorithm developed in Miller [16] is derived from the two-layer L-band brightness temperature model and the continuous logistic model. The continuous logistic model is a differential equation that models the decrease in physical systems as a function of time using a set of sigmoidal curves. These curves begin at a maximum value with an initial interval of decrease that is approximately exponential. As the function approaches its minimum value, the decrease slows to approximately linear. When the function asymptotically reaches its minimum value, the decrease exponentially tails off and achieves stable values.

The continuous logistic model is described by a differential equation known as the logistic equation

$$\frac{dx}{dt} = \zeta x(1-x) \quad (3)$$

that has the solution

$$x(t) = \frac{1}{1 + \left(\frac{1}{x_o} - 1\right) e^{\zeta t}}, \quad (4)$$

where x_o is the function's initial value, ζ is the function's exponential rate of decrease, and t is time. The function $x(t)$ is known as the sigmoid function.

The empirical algorithm uses SMAP rSIR T_V^B image time series and the sigmoid function. For each rSIR grid cell within the percolation facies spatial extent defined by the two-layer L-band brightness temperature model, we first normalize T_V^B

time series

$$T_{V,N}^B(t) = \frac{T_V^B(t) - T_{V,min}^B}{T_{V,max}^B - T_{V,min}^B}, \quad (5)$$

where $T_{V,min}^B$ is the minimum vertically-polarized brightness temperature, and $T_{V,max}^B$ is the maximum vertically-polarized brightness temperature. Similar to the firn saturation parameter calculation procedure, we calculate $T_{V,min}^B$ and $T_{V,max}^B$ by smoothing T_V^B time series, and then estimating the minimum and maximum values. We then calculate the exponential rate of decrease by iteratively applying the sigmoid fit

$$T_{V,N}^B(t \in [t_{max}, t_{min}]) = \frac{1}{1 + \left(\frac{1}{T_{V,N}^B(t_{max})} - 1\right) e^{\zeta t}}. \quad (6)$$

$T_{V,N}^B(t \in [t_{max}, t_{min}])$ is the normalized vertical-polarization brightness temperature time series partitioned on the time interval $t \in [t_{max}, t_{min}]$, where t_{max} is the time the function achieves its maximum value, and t_{min} is the time the function achieves its minimum value. The initial normalized vertical-polarization brightness temperature $T_{V,N}^B(t_{max})$ is the function's maximum value. The final normalized vertical-polarization brightness temperature $T_{V,N}^B(t_{min})$ is the function's minimum value.

The empirical algorithm is calibrated by correlating $T_{V,min}^B$, $T_{V,max}^B$, ζ values calculated using the two-layer L-band brightness temperature model, and ζ values calculated using the continuous logistic model, with perennial firn aquifer and ice slab detections (2010–2017) [32], [26] identified via the Center for Remote Sensing of Ice Sheets (CReSIS) Accumulation Radar and the Multichannel Coherent Radar Depth Sounder flown by NASA's OIB campaigns (Fig. 1b) [19]. The calibration parameter intervals used in the empirical algorithm are given in Table I. If the calculated calibration parameters are within the intervals, the rSIR grid cell is converted to a binary parameter to map the total spatial extent of ice slab and perennial firn aquifer areas. For a complete physical description of ice slabs and perennial firn aquifers within the Greenland Ice Sheet, and additional details on the empirical algorithm and the associated uncertainty, see Miller [16].

[TABLE 1 about here.]

D. Regional Atmospheric Climate Model

The Regional Atmospheric Climate Model (RACMO2) is a limited-area atmospheric circulation model from which a polar version (p) has been developed to simulate the climate over the polar ice sheets. It includes a multi-layer firn model that includes snow thermodynamics, and allows for surface melting, vertical percolation, retention and refreezing, and run-off [44]. Snow albedo is simulated as a function of snow grain size, cloud cover, solar zenith angle, and impurity concentration [45]. RACMO2 also includes drifting, snow erosion, and sublimation [46]. Here, we use simulations from the most recent model version (RACMO2.3p2), which features updates in cloud physics, and an improved representation of impurity concentration, refreezing, albedo, and snowdrift [18]. RACMO2.3p2 simulations are currently generated at 5.5 km

horizontal resolution between 1958 and 2019 on a domain covering the Greenland Ice Sheet. The model is forced at its lateral boundaries by six-hourly ERA-40 [47], ERA-Interim [48], and ERA5 [49] reanalyses.

Snow accumulation simulations are projected on a Northern Hemisphere EASE-Grid 2.0 at a 3.125 km grid cell spacing, and then ice sheet-masked using the GIMP Land Ice and Ocean Classification Mask, Version 1, Data Set [43]. We then calculate a climatological snow accumulation estimate between 1 April 2010 and 31 March 2019 for each rSIR grid cell within the percolation facies spatial extent.

E. NASA's Operation IceBridge Campaigns

The CReSIS Accumulation Radar was flown over Greenland on a P-3 aircraft in April and May between 2010 and 2017 as part of NASA's OIB campaigns [19]. The instrument operates at a center frequency of 750 MHz with a bandwidth of 300 MHz, resulting in a range resolution in firn of 0.5 m [50]. The collected observations have an along-track resolution of approximately 30 m with 15 m spacing between traces in the final processed radargrams. At a nominal flight altitude of 500 m above the ice sheet surface, the cross-track resolution varies between 20 m for a smooth surface and 54 m for a rough surface with no appreciable layover.

We construct radargram profiles over southwestern and southeastern Greenland. Each profile was collected prior to melt onset over a transect extending from the dry snow facies to the percolation facies. The southwestern profile was collected 5 May 2017 (transect A-B; Fig. 1). The southeastern profile was collected 22 April 2017 (transect C-D; Fig. 1). We use a first maximum after maximum gradient re-tracker to identify the surface return in each profile, and flatten each profile so that the depth axis is measured relative to the local surface elevation. The large change in surface elevation over the length of each profile makes it impractical to display these images in an elevation-corrected format. The radargrams are then incoherently averaged an additional 15 times along-track to improve the visual interpretability at scale. This results in a final along-track trace spacing of 225 m. Surface elevation profiles are calculated by subtracting the radar's flight clearance over the ice sheet surface from the aircraft's global positioning system altitude, and then smoothed using a 100-observation temporal averaging window to a horizontal resolution of 1.5 km.

In the dry snow facies, the penetration depth is approximately 1 km in the cold snow and firn layers, and underlying glacial ice. However, the penetration depth is reduced to between meters and tens of meters in the warmer percolation facies by higher attenuation in the ice column, scattering from embedded ice structures and spatially coherent melt layers, and most significantly, by reflection at the upper surface of meltwater stored within perched and perennial firn aquifers, and buried supraglacial lakes.

IV. RESULTS

A. GRD and rSIR Firn Saturation Parameter Mappings

Fig. 2 and Fig. 3 show the firn saturation parameter (2015–2019) mapped over the percolation facies using the SMAP

GRD and rSIR T_V^B image time series and the two-layer L-band brightness temperature model. The total initial ice-masked spatial extent is $1.85 \times 10^6 \text{ km}^2$ for the GRD mapping (Fig. 2a), and $1.80 \times 10^6 \text{ km}^2$ for the rSIR mapping (Fig. 2b). Image reconstruction refines the ice sheet-land, ice sheet-ocean, and surrounding ice cap boundaries as well as the percolation facies-dry snow facies boundaries, which reduces Greenland's total initial ice-masked spatial extent by 50,000 km^2 (3%). The total spatial extent of the percolation facies is $5.84 \times 10^5 \text{ km}^2$ for the GRD mapping, and $5.75 \times 10^5 \text{ km}^2$ for the rSIR mapping. The percolation facies-dry snow facies and wet snow facies-percolation facies boundaries are also refined, which reduces the total percolation facies spatial extent by 9,000 km^2 (2%).

[Fig. 2 about here.]

[Fig. 3 about here.]

The firn saturation parameter values exhibit spatial patterns that are consistent in both the GRD and the rSIR mappings (Fig. 2, Fig. 3). Higher firn saturation parameter values are mapped over south eastern, southern, and north western Greenland. Variable firn saturation parameter values are mapped over western, northern, and north eastern Greenland. However, while the spatial patterns are consistent, the firn saturation parameter in the rSIR mapping achieves higher values as compared to the GRD mapping. This is a result of the refinement in the percolation facies boundaries, and the corresponding reduction in mixed emission within the percolation facies spatial extent. Maximum firn saturation parameter values of $\xi_{max}=1.26$ are exhibited in the GRD mapping (Fig. 2a). The mean value is $\bar{x}=0.5$, and the standard deviation is $\sigma=\pm 0.21$. Maximum firn saturation parameter values of $\xi_{max}=2.8$ are exhibited in the rSIR mapping (Fig. 2b). The mean value is $\bar{x}=0.6$, and the standard deviation is $\sigma=\pm 0.28$. The rSIR mapping also exhibits tighter closed-contour intervals with higher firn saturation parameter values, especially in south eastern (Fig. 3c, d) and southern Greenland, and steeper contour gradients. We infer that closed-contour intervals indicate thicker water-saturated firn layers with larger volumetric fractions of meltwater that are relatively uniform over expansive areas. We also infer that steeper contour gradients indicate spatial variability in the thickness and volumetric fraction of meltwater stored within the water-saturated firn layers over limited areas.

Our results indicate that the firn saturation parameter calculated from the SMAP rSIR T_V^B imagery effectively resolves boundaries and spatial patterns of water-saturated firn layers within the percolation facies that are not effectively resolved in SMAP GRD T_V^B imagery, and therefore improves the accuracy of the mapping.

B. rSIR Firn Saturation Parameter Mapping Comparisons

Fig. 4–Fig. 6 show the firn saturation parameter (2015–2019) together with ice slab and perennial firn aquifer spatial extents (2015–2019) mapped using the SMAP rSIR T_V^B image time series and the empirical algorithm, and snow accumulation estimates (2010–2019) simulated via RACMO2.3. We

note that exact snow accumulation ranges within the ice slab and perennial firn aquifer spatial extents are challenging to resolve as a result of the mismatch between the effective resolution of SMAP (~ 18 km) and the horizontal resolution of RACMOp2.3 (5.5 km). Although image reconstruction improves SMAP's effective resolution, it still spans a spatial extent more than three times the horizontal resolution of RACMOp2.3. Snow accumulation distributions within each of the sub-facies are difficult to interpret, especially at the percolation facies-dry snow facies and the wet snow facies-percolation facies boundaries. The spatial patterns are in general agreement. However, the firn saturation parameter is often shifted slightly upslope of higher snow accumulation areas throughout the percolation facies.

[Fig. 4 about here.]

[Fig. 5 about here.]

[Fig. 6 about here.]

Fig. 7 shows a scatterplot of the firn saturation parameter values versus snow accumulation. MacFerrin [26] previously reported that snow accumulation is less than 572 ± 32 mm w.e. yr⁻¹ in ice slab areas. Forster [31] reported that snow accumulation exceeds 800 mm w.e. yr⁻¹ in perennial firn aquifer areas. Here, we find an unreasonably wide range of snow accumulation estimates in each of the sub-facies. Fig. 7 illustrates the complexities of interpreting grid cell comparisons between satellite-derived mappings of geophysical parameters that often include significant uncertainty in the mapped spatial extents [16] and regional climate model-derived simulations.

[Fig. 7 about here.]

The ice slab spatial extent extends over 76,000 km² (13%) of the percolation facies, and is primarily mapped over lower snow accumulation areas in central eastern, southern, western, and northern Greenland (Fig. 4, Fig. 5). The perennial firn aquifer spatial extent extends over 64,000 km² (11%) of the percolation facies, and is primarily mapped over higher snow accumulation areas in southeastern, southern, and northwestern Greenland (Fig. 4, Fig. 6). Additional scattered perennial firn aquifer areas are mapped over central eastern, central western, and northern Greenland, where snow accumulation is significantly decreased. Combined, these sub-facies are the equivalent of 24% of the percolation facies.

The firn saturation parameter values mapped over the ice slab spatial extent range from between $\xi=0.1$ and $\xi=2.0$, (Fig. 4, Fig. 5), and exhibit distinct spatial patterns that are correlated with snow accumulation spatial patterns. Variable firn saturation parameter values are mapped in variable snow accumulation areas in western, northern, and north eastern Greenland. Closed-contour intervals indicate that the firn saturation parameter values range from between $\xi=0.4$ and $\xi=0.8$, and values generally decrease with increasing northern latitudes. A lack of closed-contour intervals and wide contour gradients indicates gradual changes in the firn saturation parameter over large areas. The firn saturation parameter values mapped over the perennial firn aquifer spatial extent

range from between $\xi=0.2$ and $\xi=2.8$, and similar to ice slabs areas, exhibit spatial patterns that are correlated with snow accumulation spatial patterns (Fig. 4, Fig. 5). The highest firn saturation parameter values are mapped over the highest snow accumulation areas in southeastern Greenland (Fig. 5). Closed-contour intervals indicate several expansive perennial firn aquifer areas where the firn saturation parameter values exceed $\xi=1.8$. These areas include locations mapped above Midgard, Helheim, Ikertivaq, and Køge Bugt glaciers (Fig. 8). Steep contour gradients surround these closed-contour intervals, indicating rapid decreases in the firn saturation parameter values over limited areas. Higher firn saturation parameter values are mapped over higher snow accumulation areas in southern and northwestern Greenland. Closed-contour intervals indicate that the firn saturation parameter values range from between $\xi=1.0$ and $\xi=1.6$, and values generally decrease with increasing northern latitudes. Wider contour gradients surround these closed contour intervals, indicating more gradual decreases in the firn saturation parameter values over larger areas. The lowest firn saturation parameter values are mapped over the lowest snow accumulation areas in central eastern, central western, and northern Greenland. Contour gradients widen with decreasing firn saturation parameter values.

[Fig. 8 about here.]

Fig. 9 shows the firn saturation parameter values (2015–2019) together with the CReSIS Accumulation Radar southwestern (5 May 2017) and southeastern (22 April 2017) profiles collected as part of NASA's OIB campaigns. Surface elevation ranges from between ~ 1700 and 2500 m a.s.l in the southwestern profile, and between ~ 1500 and 2500 m a.s.l. in the southeastern profile. These radargram profiles display ice sheet stratigraphy in the dry snow facies and the percolation facies just prior to the melting season. Exceptionally bright surface-parallel reflectors that represent spatially coherent melt layers formed during recent extreme [52] and anomalous [51] melting seasons are exhibited throughout the upper firn layers of the radargram profiles [24]. The large dielectric contrast between the spatially coherent melt layers and the overlying, underlying, and interior firn layers results in high-reflectivity at the interfaces. However, electromagnetic energy still propagates through the high-reflectivity spatially coherent melt layers into the deeper firn layers.

[Fig. 9 about here.]

The dry snow facies exhibit an alternating sequence of bright and dark surface-parallel reflectors that represent seasonal snow accumulation layers throughout the depth range displayed in both the southwestern and the southeastern profiles. Small density differences between summer and winter snow accumulation results in dielectric contrasts and interface reflectivity [53]. Upward dipping layers transitioning to relatively flat layers in the southwestern profile indicate decreases in snow accumulation towards the ice sheet periphery. Downward dipping layers in the southeastern profile indicate large increases in snow accumulation towards the ice sheet periphery. The snow accumulation patterns exhibited in the radargram profiles are generally consistent with snow

accumulation patterns simulated by RACMOp2.3 (Fig. 4c–Fig. 6c). The firn saturation parameter value is $\xi=0$ over the dry snow facies, and extends downslope ~ 80 km (2500 m a.s.l.) in the southwestern profile, and ~ 100 km (2300 m a.s.l.) in the southeastern profile. These surface elevations represent the dry snow line (2015–2019) in the radargram profiles.

The higher-elevation percolation facies exhibit a faded alternating sequence of surface parallel reflectors that extend downslope ~ 120 km (2450 m a.s.l.) in the southwestern profile, and ~ 180 km (2100 m a.s.l.) in the southeastern profile. Firn layers warm further downslope where deep vertical percolation of seasonal meltwater occurs, and the volumetric fraction of embedded ice structures increases. Penetration depth decreases, and surface-parallel reflectors gradually disappear. The firn saturation parameter values increase at the dry snow line. The rate of increase over the southwestern profile is approximately one third the rate of increase over the southeastern profile.

The lower-elevation southwestern profile exhibits thick dark surface-parallel regions of low reflectivity that represent ice slabs (Fig. 9b). The large dielectric contrast between ice slabs and the overlying and underlying firn layers results in high reflectivity at the interfaces. However, electromagnetic energy is not scattered or absorbed within the homogeneous ice slab, it instead propagates downward through the layer and into the deeper firn layers. Ice slabs extend downslope ~ 50 km (1500–2100 m a.s.l.), range in depth from between ~ 1 and 15 m beneath the ice sheet surface, and in thickness from between ~ 5 and 20 m. The firn saturation parameter reaches the maximum value ($\xi=0.6$) upslope ~ 220 km (1700 m a.s.l.) of the ice slabs, and then decreases across the ice slabs towards the percolation facies boundary where meltwater runoff occurs. The lower-elevation southeastern profile exhibits a bright lower reflector that undulates with the local topographic gradient underneath which reflectors are absent (Fig. 9d). The lower reflector represents the upper surface of meltwater stored within a perennial firn aquifer. The large dielectric contrast between the refrozen and the water-saturated firn layer results in high reflectivity at the interface. The perennial firn aquifer extends downslope ~ 35 km (1700–2000 m a.s.l.), and ranges in depth from between ~ 10 and 30 m beneath the ice sheet surface. The firn saturation parameter reaches the maximum value ($\xi=1.8$) downslope ~ 220 km (1700 m a.s.l.) over the perennial firn aquifer, and then decreases towards the percolation facies boundary where meltwater runoff or crevasse drainage occurs.

V. DISCUSSION

The simple two-layer L-band brightness temperature model does not adequately describe the physics controlling L-band emission over areas of the percolation facies where heterogeneous vertical and lateral percolation of seasonal meltwater into porous snow and firn layers at depth results in the presence of subsurface meltwater during the melting season. Field measurements collected in and southwestern [21] and southeastern [31] Greenland suggest seasonal meltwater is capable of vertical percolation to depths greater than 10 m beneath the ice sheet surface. When the volumetric fraction

of meltwater stored within the water-saturated firn layer is $m_v=1\%$, the theoretical L-band penetration depth is estimated to be approximately 10 m [16]. This estimate is consistent with the L-band penetration depth in damp temperate firn derived from airborne interferometric synthetic aperture radar and laser altimetry observations (10 ± 4 m) [54]. To overcome capillary trapping and initiate vertical percolation, the required volumetric fraction of meltwater stored within the water-saturated firn layer is estimated to be no more than $m_v=7\%$ [55]. At $m_v=7\%$, the theoretical L-band penetration depth is reduced to less than 1 m [16]. Thus, as observed depth-integrated over SMAP's antenna footprint (i.e. ~ 18 km effective resolution), the firn saturation parameter is likely underestimated once seasonal meltwater stored within the water-saturated firn layer exceeds the volumetric fraction required to initiate vertical percolation.

Perennial firn aquifers represent radiometrically cold subsurface meltwater reservoirs that exist at depths of between 1 and 40 m [32] beneath the ice sheet surface during the freezing season [15]. The mean depth is 22 m [32]. The thickness of the water-saturated firn layer ranges from between 4 and 25 m [30], [33]. The mean thickness is 14 m [29]. Field measurements collected in southeastern Greenland suggest that the volumetric fraction of meltwater stored within the pore space of perennial firn aquifers may be as high as 25% [29], which results in high permittivity. ($\epsilon_r \approx 9 + 1i$) that limits the transmission of electromagnetic radiation (10%) to the upper firn layers [15]. L-band emissions upwelling from below the upper surface of meltwater stored within the perennial firn aquifer are extinguished by reflection at the water-saturated layer interface. During the melting season, seasonal meltwater must percolate vertically from the surface to the subsurface to recharge the perennial firn aquifer [27]. The total thickness of the water-saturated firn layer includes the thickness of the seasonal water-saturated firn layer plus the thickness of the perennial firn aquifer. Plausible thicknesses range roughly between 5 and 65 m. The mean thickness is 36 m. Thus, the firn saturation parameter is likely further underestimated over the perennial firn aquifer spatial extent, even at $m_v=1\%$.

Similar to Jezek [34], we hypothesize the complex interplay between physical temperature, the volumetric fraction of meltwater stored within the water-saturated firn layers, and latent heat also dominates depth-integrated L-band emission over perennial firn aquifer areas during the melting season. While perennial firn aquifers are radiometrically cold, the slow refreezing of deeper firn layers saturated with large volumetric fractions of meltwater represents a significant source of latent heat that is continuously released [15]. This subsurface heat source is not present in other areas of the percolation facies. Field measurements collected in southeastern Greenland indicate that firn layers overlaying the perennial firn aquifer are at, or near, the melting point year-round [29]. Our hypothesis is also consistent with temporal L-band signatures observed over the perennial firn aquifer spatial extent, which are radiometrically warm in the absence of seasonal meltwater during the freezing season (Table I). Field measurements collected in ice slab areas [25], [26] and in other areas of the percolation facies [21] in southwestern Greenland indicate that firn layers are colder as compared to perennial firn aquifer areas during

the freezing season. Temporal L-band signatures observed over the ice slab spatial extent and over other areas of the percolation facies spatial extent are also radiometrically colder as compared to temporal L-band signatures over the perennial firn aquifer spatial extent (Table I).

While the total thickness and volumetric fraction of meltwater stored within water-saturated firn layers is likely underestimated over much of the perennial firn aquifer spatial extent by the simple two-layer L-band brightness temperature model, the firn saturation parameter effectively identifies expansive englacial reservoirs that store significant volumes of meltwater year-round. Especially interesting are the locations mapped above the fast-flowing ($>100 \text{ m yr}^{-1}$) Helheim and Køge Bugt glaciers in southeastern Greenland. These large marine-terminating outlet glaciers were the second and fourth largest contributors of ice discharge from the Greenland Ice Sheet to the ocean between 1986 and 2020, respectively [56]. Recent modeling studies suggest that if perennial firn aquifers intersect with crevasse fields and contain a sufficient volume of meltwater, they are capable of initiating meltwater-induced hydrofracturing [57] through the full-thickness ($\sim 1000 \text{ m}$) of the Greenland Ice Sheet [58]. Meltwater-induced hydrofracturing is capable of delivering meltwater stored in englacial reservoirs to the subglacial hydrological system, which may lead to the localized acceleration of outlet glaciers [59], [60], peripheral ice discharge [61], and mass loss to the ocean [62].

VI. SUMMARY AND FUTURE WORK

In this study we have demonstrated the novel use of the L-band microwave radiometer on NASA's SMAP satellite for mapping firn saturation over the percolation facies of the Greenland Ice Sheet from space. We have derived a firn saturation parameter from a simple two-layer L-band brightness temperature model that can be used to estimate the spatial variability in the thickness and volumetric fraction of meltwater stored within the firn pore space. We have demonstrated that as compared to conventionally processed SMAP GRD T_V^B imagery, enhanced-resolution SMAP rSIR T_V^B imagery improves the accuracy of the firn saturation parameter mapping. We have also demonstrated that spatial variability in the firn saturation parameter is correlated with the locations of SMAP- and NASA OIB-derived englacial hydrological features (i.e., ice slabs and perennial firn aquifers) as well as RACMO2.3-simulated snow accumulation patterns. Further interpretation suggests that the firn saturation parameter likely underestimates the total thickness and volumetric fraction of meltwater stored within the water-saturated firn layers, however, effectively identifies expansive englacial reservoirs in locations that are potentially vulnerable to meltwater-induced hydrofracturing and accelerated outlet glacier flow year-round.

Future work will focus on expanding these results using individual years of enhanced-resolution SMAP rSIR T_V^B imagery to resolve spatiotemporal variability in the firn saturation parameter over the percolation facies. Given snow accumulation is a key climate parameter defining firn saturation (i.e., it seasonally controls firn pore space) as well as the formation, continued presence, and expansion of ice slabs and perennial

firn aquifers, we will attempt to resolve the uncertainties in the estimates of snow accumulation simulated via RACMO2.3 and derive more accurate estimates in the percolation facies and in each of the sub-facies. Comparisons between yearly firn saturation parameter maps and satellite-derived ice flow may provide interesting new insights into the currently unknown influence of perennial firn aquifers on the overall mass balance and stability of the Greenland Ice Sheet.

VII. ACKNOWLEDGMENTS

J. Z. Miller would like thank K. C. Jezek for providing a discussion and initial study on modeling L-band emissions over perennial firn aquifers. The authors would also like to thank P. Kuipers Munneke and M. R. van den Broeke for the RACMO2.3 snow accumulation simulations. The authors acknowledge the use of data from CReSIS generated with support from the University of Kansas, NASA Operation IceBridge (NNX16AH54G), NSF (ACI-1443054, OPP-1739003, IIS-1838230), Lilly Endowment Incorporated, and Indiana METACyt Initiative.

REFERENCES

- [1] D. M. Le Vine, G. S. E. Lagerloef, F. R. Colomb, S. H. Yueh, and F. A. Pellerano, "Aquarius: An instrument to monitor sea surface salinity from space," *IEEE Transactions on Geoscience and Remote Sensing*, vol. 45, no. 7, pp. 2040–2050, 2007.
- [2] Y. H. Kerr, P. Waldteufel, J. P. Wigneron, J. Martinuzzi, J. Font, and M. Berger, "Soil moisture retrieval from space: the soil moisture and ocean salinity (SMOS) mission," *IEEE Transactions on Geoscience and Remote Sensing*, vol. 39, no. 8, pp. 1729–1735, 2001.
- [3] D. Entekhabi, S. Yueh, P. E. O'Neill, K. H. Kellogg, A. Allen, R. Bindlish, et al., "SMAP handbook—soil moisture active passive: Mapping soil moisture and freeze/thaw from space," Jet Propulsion Laboratory, Pasadena, CA, USA, Tech. Rep. JPL CL#14-2285, 2014.
- [4] K. C. Jezek, J. T. Johnson, M. R. Drinkwater, G. Macelloni, L. Tsang, M. Aksoy, and M. Durand, "Radiometric approach for estimating relative changes in intraglacier average temperature," *IEEE Transactions on Geoscience and Remote Sensing*, vol. 53, no. 1, pp. 134–143, 2015.
- [5] G. Macelloni, M. Leduc-Leballeur, F. Montomoli, M. Brogioni, C. Ritz, and G. Picard, "On the retrieval of internal temperature of Antarctica ice sheet by using SMOS observations," *Remote Sensing of Environment*, vol. 233, p. 111405, 2019.
- [6] T. L. Mote and M. R. Anderson, K. C. Kuivinen, and C. M. Rowe, "Passive microwave-derived spatial and temporal variations of summer melt on the Greenland ice sheet," *Annals of Glaciology*, vol. 17, pp. 233–238, 1993.
- [7] W. Abdalati and K. Steffen, "Passive microwave-derived snow melt regions on the Greenland ice sheet," *Geophysical Research Letters*, vol. 22, no. 7, pp. 787–790, 1995.
- [8] M. Joshi, C. J. Merry, K. C. Jezek, and J. F. Bolzan, "An edge detection technique to estimate melt duration, season and melt extent on the Greenland Ice Sheet using passive microwave data," *Geophysical Research Letters*, vol. 28, no. 18, pp. 3497–3500, 2001.
- [9] I. S. Ashcraft and D. G. Long, "Comparison of methods for melt detection over Greenland using active and passive microwave measurements," *International Journal of Remote Sensing*, vol. 27, no. 12, pp. 2469–2488, 2006.
- [10] D. Houtz, R. Naderpour, M. Schwank, and K. Steffen, "Snow wetness and density retrieved from L-band satellite radiometer observations over a site in the west Greenland ablation zone," *Remote Sensing of Environment*, vol. 235, p. 111361, 2019.
- [11] M. Leduc-Leballeur, G. Picard, G. Macelloni, A. Mialon, and Y. H. Kerr, "Melt in Antarctica derived from soil moisture and ocean salinity (SMOS) observations at L band," *The Cryosphere*, vol. 14, no. 2, pp. 539–548, 2020.
- [12] D. Houtz, C. Mätzler, R. Naderpour, M. Schwank, and K. Steffen, "Quantifying surface melt and liquid water on the Greenland Ice Sheet using L-band radiometry," *Remote Sensing of Environment*, vol. 256, p. 112341, 2021.

- [13] M. Mousavi, A. Colliander, J. Z. Miller, D. Entekhabi, J. T. Johnson, C. A. Shuman, J. S. Kimball, and Z. R. Courville, "Evaluation of surface melt on the Greenland Ice Sheet Using SMAP L-band microwave radiometry," *IEEE Journal of Selected Topics in Applied Earth Observations and Remote Sensing*, vol. 14, pp. 11439–11449, 2021.
- [14] M. Mousavi, A. Colliander, J. Z. Miller, and J. S. Kimball, "A Novel Approach to Map the Intensity of Surface Melting on the Antarctica Ice Sheet using SMAP L-Band Microwave Radiometry," *IEEE Journal of Selected Topics in Applied Earth Observations and Remote Sensing*, to appear, pg. 1, 2022.
- [15] J. Z. Miller, D. G. Long, K. C. Jezek, J. T. Johnson, M. J. Brodzik, C. A. Shuman, L. S. Koenig, and T. A. Scambos, "Brief communication: Mapping Greenland's perennial firn aquifers using enhanced-resolution L-band brightness temperature image time series," *The Cryosphere*, vol. 14, no. 9, pp. 2809–2817, 2020.
- [16] J. Z. Miller, R. Culberg, D. G. Long, and C. A. Christopher, D. M. Schroeder and M. J. Brodzik, "An empirical algorithm to map perennial firn aquifers and ice slabs within the Greenland Ice Sheet using satellite L-band microwave radiometry," *The Cryosphere*, vol. 16, no. 1, pp. 103–125, 2022.
- [17] D. G. Long, M. Brodzik, and M. Hardman, "Enhanced resolution SMAP brightness temperature image products," *IEEE Transactions Geoscience and Remote Sensing*, vol. 57, no. 7, pp. 4151–4163, 2019.
- [18] B. Noël, W. J. van de Berg, J. M. van Wessem, E. van Meijgaard, D van As, J.T. Lenaerts, S. Lhermitte, P.K. Munneke, C. J. P. P. Smeets and L. H. van Ulft, R. S. W. van de Wall, and M. R. van den Broeke, "Modelling the climate and surface mass balance of polar ice sheets using RACMO2-Part 1: Greenland (1958–2016)," *The Cryosphere*, vol. 12, no. 3, pp. 811–831, 2018.
- [19] F. Rodriguez-Morales, S. Gogineni, C. J. Leuschen, J. D. Paden, J. Li, C. C. Lewis, B. Panzer, D. Gomez-Garcia Alvestegui, A. Patel, K. Byers, R. Crowe, K. Player, R. D. Hale, E. J. Arnold, L. Smith, C. M. Gifford, D. Braaten, and C. Panton, "Advanced multifrequency radar instrumentation for polar research," *IEEE Transactions on Geoscience and Remote Sensing*, vol. 52, no. 5, pp. 2824–2842, 2014.
- [20] W. T. Pfeffer and N. F. Humphrey, "Formation of ice layers by infiltration and refreezing of meltwater," *Annals of Glaciology*, vol. 26, pp. 83–91, 1998.
- [21] N. F. Humphrey, J. T. Harper, W. T. Pfeffer, "Thermal tracking of meltwater retention in Greenland's accumulation area," *Journal of Geophysical Research: Earth Surface*, no. F1, 2012.
- [22] J. Harper, N. Humphrey, W. T. Pfeffer, J. Brown, and X. Fettweis, "Greenland ice—sheet contribution to sea—level rise buffered by meltwater storage in firn," *Nature (London)*, vol. 491, no. 7423, pp. 240–243, 2012.
- [23] C. S. Benson, "Stratigraphic studies in the snow and firn of the Greenland ice sheet," Ph.D. dissertation, California Institute of Technology, 1960.
- [24] R. Culberg, D. M. Schroeder, and W. Chu, "Extreme melt season ice layers reduce firn permeability across Greenland," *Nature communications*, vol. 12, no. 1, pp. 2336–2336, 2021.
- [25] H. Machguth, M. Macferrin, D. Van As, J. E. Box, C. Charalampidis, W. Colgan, R. S. Fausto, H. A. J. Meijer, E. Mosley-thompson, and S. Van De Wal, Roderik, "Greenland meltwater storage in firn limited by near-surface ice formation," *Nature Climate Change*, vol. 6, no. 4, pp. 390–393, 2016.
- [26] M. MacFerrin, H. Machguth, D. van As, C. Charalampidis, C. M. Stevens, A. Heilig, B. Vandecrux, P. L. Langen, R. Mottram, X. Fettweis, M. van den Broeke, W. T. Pfeffer, M. S. Moussavi, and W. Abdalati, "Rapid expansion of Greenland's low-permeability ice slabs," *Nature*, vol. 573, no. 774, pp. 403–407, 407A–407G, 2019.
- [27] A. G. Fountain and J. S. Walder, "Water flow through temperate glaciers," *Reviews of Geophysics*, vol. 36, no. 3, pp. 299–328, 1998.
- [28] N. F. Humphrey, J. T. Harper, and T. W. Meierbacholt, "Physical limits to meltwater penetration in firn," *Journal of Glaciology*, p. 1–9, 2021.
- [29] L. S. Koenig, C. Miège, R. R. Forster, and L. Brucker, "Initial in situ measurements of perennial meltwater storage in the Greenland firn aquifer," *Geophysical Research Letters*, vol. 41, no. 1, pp. 81–85, 2014.
- [30] L. N. Montgomery, N. Schmerr, S. Burdick, R. R. Forster, L. Koenig, A. Legchenko, S. Ligtenberg, C. Miège, O. L. Miller, and D. K. Solomon, "Investigation of firn aquifer structure in southeastern Greenland using active source seismology," *Frontiers in Earth Science*, vol. 5, p. 10, 2017.
- [31] R. R. Forster, J. E. Box, M. R. Van Den Broeke, C. Miège, E. W. Burgess, H. Van Angelen, Jan, J. T. M. Lenaerts, L. S. Koenig, J. Paden, C. Lewis, S. P. Gogineni, C. Leuschen, and J. R. McConnell, "Extensive liquid meltwater storage in firn within the Greenland ice sheet," *Nature Geoscience*, vol. 7, no. 2, pp. 95–98, 2014.
- [32] C. Miège, R. R. Forster, L. Brucker, L. S. Koenig, D. K. Solomon, J. D. Paden, J. E. Box, E. W. Burgess, J. Z. Miller, L. McNerney, N. Brautigam, R. S. Fausto, and S. Gogineni, "Spatial extent and temporal variability of Greenland firn aquifers detected by ground and airborne radars," *Journal of Geophysical Research: Earth Surface*, vol. 121, no. 12, pp. 2381–2398, 2016.
- [33] W. Chu, D. M. Schroeder, and M. R. Siegfried, "Retrieval of englacial firn aquifer thickness from ice-penetrating radar sounding in south-eastern Greenland," *Geophysical Research Letters*, vol. 45, no. 21, pp. 11,770–11,778, 2018.
- [34] K. C. Jezek, "Preliminary model for L-band emissions from a perennial firn aquifer," personal communication, 2011.
- [35] B. R. Hicks and D. G. Long, "Inferring Greenland melt and refreeze severity from SeaWinds scatterometer data," *International Journal of Remote Sensing*, vol. 32, no. 23, pp. 8053–8080, 2011.
- [36] J. Piepmeyer, P. Mohammed, G. De Amici, E. Kim, J. Pen, and C. Ruf, "Algorithm theoretical basis document (ATBD) SMAP calibrated, time-ordered brightness temperatures L1b_TB data product," Jet Propulsion Laboratory, Pasadena, CA, USA, Tech. Rep., 2014.
- [37] D. G. Long and M. J. Brodzik, "Optimum image formation for space-borne microwave radiometer products," *IEEE Transactions Geoscience and Remote Sensing*, vol. 54, no. 5, pp. 2763–2779, 2016.
- [38] D. S. Early and D. G. Long, "Image reconstruction and enhanced resolution imaging from irregular samples," *IEEE Transactions on Geoscience and Remote Sensing*, vol. 39, no. 2, pp. 291–302, 2001.
- [39] D. G. Long and D. L. Daum, "Spatial resolution enhancement of SSM/I data," *IEEE Transactions on Geoscience and Remote Sensing*, vol. 36, no. 2, pp. 407–417, 1998.
- [40] M. J. Brodzik, B. Billingsley, T. Haran, B. Raup, and M. H. Savoie, "EASE-Grid 2.0: Incremental but significant improvements for Earth-gridded data sets," *ISPRS International Journal of Geo-Information*, vol. 1, no. 1, pp. 32–45, 2012.
- [41] M. Tiuri, A. Sihvola, E. Nyfors, and M. Hallikainen, "The complex dielectric constant of snow at microwave frequencies," *IEEE Journal of Oceanic Engineering*, vol. 9, pp. 377–382, 1984.
- [42] F. T. Ulaby and D. G. Long, *Microwave Radar and Radiometric Remote Sensing*, University of Michigan Press, Ann Arbor, Michigan, 2014.
- [43] I.M. Howat, A. Negrete, and B. E. Smith, "The Greenland ice mapping project (GIMP) land classification and surface elevation data sets," *The Cryosphere*, vol. 8, no. 4, pp. 1509–1518, 2014.
- [44] J. Ettema, M. R. Broeke, E. van Meijgaard, and W. J. v. de Berg, "Climate of the Greenland Ice Sheet using a high-resolution climate model - part 2: Near-surface climate and energy balance," *The Cryosphere*, vol. 4, no. 4, p. 529, 2010.
- [45] P. Kuipers Munneke, C. H. Reijmer, and M. R. van den Broeke, "Assessing the retrieval of cloud properties from radiation measurements over snow and ice," *International Journal of Climatology*, vol. 31, no. 5, pp. 756–769, 2011.
- [46] J. T. M. Lenaerts, M. R. Broeke, J. H. van Angelen, E. van Meijgaard, and S. J. Déry, "Drifting snow climate of the Greenland Ice Sheet: a study with a regional climate model," *The Cryosphere*, vol. 6, no. 4, p. 891, 2012.
- [47] S. M. Uppala, et al., "The ERA-40 re-analysis," *Quarterly Journal of the Royal Meteorological Society*, vol. 131, no. 612, pp. 2961–3012, 2005.
- [48] D. P. Dee, et al., "The ERS-Interim reanalysis: configuration and performance of the data assimilation system," *Quarterly Journal of the Royal Meteorological Society*, vol. 137, no. 656, pp. 553–597, 2011.
- [49] H. Hersbach, et al., "The ERA5 Global Reanalysis," *Quarterly Journal of the Royal Meteorological Society*, vol. 146, no. 730, p. 1999–2049, 2020.
- [50] G. Lewis, E. Osterberg, R. Hawley, B. Whitmore, H. P. Marshall and J. E. Box, "Regional Greenland accumulation variability from Operation IceBridge airborne accumulation radar," *The Cryosphere*, vol. 11, no. 2, pp. 773–788, 2017.
- [51] S. V. Nghiem, D. K. Hall, T. L. Mote, M. Tedesco, M. R. Albert, K. Keegan, C. A. Shuman, N. E. DiGirolamo, and G. Neumann, "The extreme melt across the Greenland Ice Sheet in 2012," *Geophysical Research Letters*, vol. 39, no. 20, 2012.
- [52] M. Tedesco, X. Fettweis, M. R. van den Broeke, R. S. van de Wal, C. J. Smeets, W. J. van de Berg, M. C. Serreze, and J. E. Box, "The role of albedo and accumulation in the 2010 melting record in Greenland," *Environmental Research Letters*, vol. 6, no. 1, pg. 014005, 2011.
- [53] R. Culberg and D. M. Schroeder, "Firn clutter constraints on the design and performance of orbital radar ice sounders," *IEEE Transactions on Geoscience and Remote Sensing*, vol. 58, no. 9, pp. 6344–6361, 2020.

- [54] E. Rignot, K. Echelmeyer and W. Krabill, "Penetration depth of interferometric synthetic-aperture radar signals in snow and ice," *Geophysical Research Letters*, vol. 28, no. 18, pp. 3501–3504, 2001.
- [55] S. C. Colbeck and E. A. Anderson, "The permeability of a melting snow cover," *Water Resources Research*, vol. 18, no. 4, pp. 904–908, 1982.
- [56] K. D. Mankoff, A. Solgaard, W. Colgan, A. P. Ahlstrom, S. A. Khan, and R. S. Fausto, "Greenland Ice Sheet solid ice discharge from 1986 through March 2020," *Earth System Science Data*, vol. 12, no. 2, pp. 1367–1383, 2020.
- [57] C. J. van der Veen, "Fracture mechanics approach to penetration of surface crevasses on glaciers," *Cold Regions Science and Technology*, vol. 27, no. 1, pp. 31–47, 1998.
- [58] K. Poinar, I. Joughin, D. Lilien, L. Brucker, L. Kehrl, and S. Nowicki, "Drainage of Southeast Greenland firn aquifer water through crevasses to the bed," *Frontiers in Earth Science (Lausanne)*, vol. 5, 2017.
- [59] T. Moon, I. Joughin, B. Smith, M. R. Broeke, W. J. Berg, B. Noel, and M. Usher, "Distinct patterns of seasonal Greenland glacier velocity," *Geophysical Research Letters*, vol. 41, no. 20, pp. 7209–7216, 2014.
- [60] L. A. Stevens, M. Nettles, J. L. Davis, T. T. Creyts, J. Kingslake, A. P. Ahlstrom, and T. B. Larsen, "Helheim Glacier diurnal velocity fluctuations driven by surface melt forcing," *Journal of Glaciology*, vol. 68, no. 267, pp. 77–89, 2021–2022.
- [61] M. King, I. Howat, S. Candela, M. Noh, J. Seongsu, B. P. Y. Brice, M. R. van den Broeke, B. Wouters, and A. Negrete, "Dynamic ice loss from the Greenland Ice Sheet driven by sustained glacier retreat," *Communications Earth and Environment*, vol. 1, no. 1, 2020.
- [62] A. Shepherd, et al., "Mass balance of the Greenland ice sheet from 1992 to 2018," *Nature (London)*, vol. 579, no. 7798, pp. 233–239, 2020.
- [63] M. J. Brodzik and D. G. Long and M. A. Hardman, "SMAP Radiometer Twice-Daily rSIR-Enhanced EASE-Grid 2.0 Brightness Temperatures, Version 1," 2019, *NASA National Snow and Ice Data Center Distributed Active Archive Center*, doi: <https://doi.org/10.5067/QZ3WJNOUZLKF>.
- [64] I.M. Howat, A. Negrete, and B. E. Smith, "MEaSUREs Greenland Ice Mapping Project (GIMP) Digital Elevation Model, Version 1," 2015, *NASA National Snow and Ice Data Center Distributed Active Archive Center*, doi: <https://doi.org/10.5067/NV34YUIXLP9W>.
- [65] T. Haran, J. Bohlander, T. A. Scambos, T. Painter, and M. Fahnestock, "MEaSUREs MODIS Mosaic of Greenland (MOG) 2015 Image Maps, Version 2," 2018, *NASA National Snow and Ice Data Center Distributed Active Archive Center*, doi:<https://doi.org/10.5067/9ZO79PHOTYE5>.
- [66] I. Joughin, "MEaSUREs Greenland Ice Sheet Mosaics from SAR Data, Version 1," 2015, *NASA National Snow and Ice Data Center Distributed Active Archive Center*, doi: <https://doi.org/10.5067/6187DQUL3FR5>.
- [67] I. Joughin, B. E. Smith, I. M. Howat, T. Moon, and T. A. Scambos, "A SAR record of early 21st century change in Greenland," *Journal of Glaciology*, vol. 62, no. 231, pp. 62–71, 2016.



Julie Z. Miller received the B.S. degree in applied mathematics and the M.S. and Ph.D. degrees in geography with a focus on microwave remote sensing of polar ice sheets from the University of Utah, Salt Lake City, UT, USA, in 2010, 2012, and 2019, respectively. She then completed a postdoctoral fellowship at Byrd Polar and Climate Research Center, The Ohio State University, Columbus, OH, USA. She is currently a Research Scientist with The Earth Science and Observation Center, Cooperative Institute for Research in Environmental Sciences (CIRES), University of Colorado, Boulder, CO, USA. She is also a member of NASA's SMAP Science Team. Her research interest focuses on developing algorithms to map surface and subsurface meltwater in Greenland and Antarctica using multifrequency microwave radiometer and radar scatterometer imagery. Dr. Miller has participated in field and airborne campaigns in both Greenland and Antarctica.



David G. Long (S'80-SM'98-F'08) obtained his Ph.D. in Electrical Engineering from the University of Southern California in 1989. From 1983 to 1990 he worked for NASA's Jet Propulsion Laboratory (JPL) where he developed advanced radar remote sensing systems. While at JPL he was the Project Engineer on the NASA Scatterometer (NSCAT) project which flew from 1996 to 1997. He also managed the SCANSAT project, the precursor to SeaWinds which was flown in 1999 on QuikSCAT, in 2002 on ADEOS-II, and in 2014 on the International Space Station. He is currently a Professor in the Electrical and Computer Engineering Department at Brigham Young University where he teaches upper division and graduate courses in communications, microwave remote sensing, radar, and signal processing and is the director of the BYU Center for Remote Sensing. He is the principal investigator on several NASA-sponsored research projects in remote sensing. He has over 400 publications in various areas including signal processing, radar scatterometry, and synthetic aperture radar. His research interests include microwave remote sensing, radar theory, space-based sensing, estimation theory, signal processing, and mesoscale atmospheric dynamics. He has received the NASA Certificate of Recognition several times and is an Associate Editor for *IEEE Geoscience and Remote Sensing Letters*.



Christopher A. Shuman is an Associate Research Professor at the University of Maryland, Baltimore County's Geography and Environmental Systems Department based at NASA Goddard Space Flight Center's Cryospheric Sciences Laboratory. He obtained his B.A. cum laude with honors in Geology from Moravian College in 1982. He obtained his M.S. and Ph.D. degrees from The Pennsylvania State University in Geology and Geoscience, respectively. From 1992 to 1994, he held a post-doctoral appointment with the Earth System Science Center and the Department of Geosciences at Penn State. From 1994 to 1999, he held post-doctoral appointments with the National Research Council and the Universities Space Research Association at NASA Goddard Space Flight Center. From 1999 to 2001, he was an Assistant Research Scientist at the Earth System Science Interdisciplinary Center at the University of Maryland. From 2001 to 2007, he was a Physical Scientist at NASA Goddard Space Flight Center and Deputy Project Scientist for the ICESat Mission (2001–2005). He has contributed to research on in situ, satellite, and modeled temperature data sets from Greenland as well as changes to Antarctic ice shelves and major outlet glaciers. Previously, he has authored or co-authored research papers on ice elevation changes and glacier mass losses using altimetry in combination with other remote sensing in the Antarctica Peninsula, on the accuracy of the first ICESat mission's data over Antarctica's large subglacial lakes. He has also worked on composite temperature records derived from automatic weather stations (AWS), passive microwave data from SMMR and SSM/I, and IR data from satellite sensors. In addition, Dr. Shuman has successfully matched those records through stratigraphic correlation with stable isotope temperature proxy profiles in shallow snow layers. He has worked extensively in Greenland (7 deployments) and Antarctica (6 field deployments plus multiple NASA Operation Ice Bridge flights from Punta Arenas, Chile). He began his cryospheric career helping to date the 3054 m long Greenland Ice Sheet Project 2's (GISP2) deep ice core in 1992.



Riley Culberg (S'19) received the B.S. degree in computer science and geospatial information science from the United States Military Academy, West Point, NY, USA in 2012, and the M.S. degree in electrical engineering from Stanford University, Stanford, CA, USA in 2019, where he is currently pursuing the PhD degree in electrical engineering. His research focuses on observing the near-surface hydrology and structure of ice sheets, ice shelves, and icy planetary bodies using ice-penetrating radar systems. He received the US Department of Defense National Defense Science and Engineering Graduate Fellowship in 2019.



Molly A. Hardman received the B.Sc. degree (Hons.) in physics from the University of KwaZulu-Natal, Durban, South Africa, in 1976, and the M.S. degree in aerospace engineering from the University of Colorado Boulder, Boulder, CO, USA, in 1991. She was with the National Snow and Ice Data Center (NSIDC), CIRES, University of Colorado Boulder, Boulder CO, USA from 1989 to 1993, and returned to work at NSIDC in 2013. In the intervening years, she worked in scientific software development, including on software that flew on the final mission of the Space Shuttle Columbia. She also owned and operated her own company manufacturing and selling high powered HF amplifiers. She is currently a Senior Associate Scientist with NSIDC where she works on software to process and analyze passive microwave data.



Mary J. Brodzik is a Senior Associate Scientist at NSIDC, CIRES, University of Colorado Boulder, Boulder, CO, USA. She obtained her B.A. summa cum laude in Mathematics from Fordham University in 1987. Her experience includes software development, validation and verification on Defense Department satellite command and control and satellite tracking systems. Since coming to NSIDC in 1993, she has implemented software systems to design, produce and analyze snow and ice data products from satellite-based visible and passive microwave imagery. She has contributed to the NSIDC data management and software development teams for the NASA Cold Lands Processes Experiment and Operation IceBridge. As principal investigator on the NASA Making Earth Science Data Records for Use in Research Environments (MEaSUREs) Calibrated Enhanced-Resolution Brightness Temperature project, she is managed the operational production of a 44-year EASE-Grid 2.0 Earth Science Data Record of satellite passive microwave data. She is using MODIS data products to derive the first systematically-derived global map of the world's glaciers. For the US Agency for International Development, she is developing snow and glacier ice melt models to better understand the contribution of glacier ice melt to major rivers with headwaters in High Asia. Her research interests include optical and passive microwave sensing of snow, remote sensing data gridding schemes, and effective ways to visualize science data.

LIST OF FIGURES

- 1 (a) 2015–2019 ice slab (cyan shading), perennial firn aquifer (blue shading), and percolation facies (purple shading) spatial extents mapped using the SMAP rSIR T_V^B image time series [63] and the empirical algorithm [16]; 2000 m a.s.l. contour (black line) and 2500 m a.s.l. contour (black dotted line) [43], [64]; 2017 CReSIS Accumulation Radar (AR) southwestern (orange line, transect A-B; Fig. 9b) and southeastern (red line, transect C-D; Fig. 9d) profiles, all overlaid on the 2015 MODIS Mosaic of Greenland [65]. Zoom boxes over southwestern (orange box; Fig. 2a-b) and southeastern (red box; Fig. 2c-d) Greenland. (b) CReSIS AR- and MCoRDS-derived 2010–2014 ice slab (cyan shading) [26] and 2010–2017 perennial firn aquifer (blue shading) [32] detections along NASA OIB flight lines (black interior lines). 13
- 2 2015–2019 firn saturation parameter spatial extent (rainbow colorscale) and contour intervals (white lines) mapped using the SMAP (a) GRD and (b) rSIR T_V^B image time series [63] and the two-layer L-band brightness temperature model [16] overlaid on the 2015 MODIS Mosaic of Greenland [65]. 14
- 3 2015–2019 firn saturation parameter spatial extent (rainbow colorscale) and contour intervals (white lines) mapped using the SMAP (a-b) GRD and (c-d) rSIR T_V^B image time series [63] and the two-layer L-band brightness temperature model [16] overlaid on the 2015 MODIS Mosaic of Greenland (zoom boxes in Fig. 1a) [65]. 15
- 4 (a) 2015–2019 firn saturation parameter spatial extent (rainbow colorscale) and contour intervals (white lines) mapped using the SMAP rSIR T_V^B image time series [63] and the two-layer L-band brightness temperature model [16]; 2000 m a.s.l. contour (black line), and the 2500 m a.s.l. contour (black dotted line) [43], [64]; 2017 CReSIS Accumulation Radar (AR) southwestern (orange line, transect A-B; Fig. 9b) and southeastern (red line, transect C-D; Fig. 9d) profiles, all overlaid on the 2015 MODIS Mosaic of Greenland [65]. (b) 2015–2019 ice slab (cyan shading), perennial firn aquifer (blue shading), and percolation facies (purple shading) spatial extents mapped using the SMAP rSIR T_V^B image time series [63] and the empirical algorithm [16]. (c) Estimates of snow accumulation (rainbow logarithmic colorscale) simulated via RACMOp2.3 [18]. 16
- 5 (a) 2015–2019 firn saturation parameter spatial extent (rainbow colorscale) and contour intervals (white lines) mapped using the SMAP rSIR T_V^B image time series [63] and the two-layer L-band brightness temperature model [16]; 2000 m a.s.l. contour (black line), and the 2500 m a.s.l. contour (black dotted line) [43], [64]; 2017 CReSIS Accumulation Radar (AR) southwestern (orange line, transect A-B; Fig. 9b) profiles, all overlaid on the 2015 MODIS Mosaic of Greenland [65] (orange zoom box; Fig. 1). (b) 2015–2019 ice slab (cyan shading), perennial firn aquifer (blue shading), and percolation facies (purple shading) spatial extents mapped using the SMAP rSIR T_V^B image time series [63] and the empirical algorithm [16]. (c) Estimates of snow accumulation (rainbow logarithmic colorscale) simulated via RACMOp2.3 [18]. 17
- 6 (a) 2015–2019 firn saturation parameter spatial extent (rainbow colorscale) and contour intervals (white lines) mapped using the SMAP rSIR T_V^B image time series [63] and the two-layer L-band brightness temperature model [16]; 2000 m a.s.l. contour (black line), and the 2500 m a.s.l. contour (black dotted line) [43], [64]; 2017 CReSIS Accumulation Radar (AR) southeastern (red line, transect C-D; Fig. 9d) profile, all overlaid on the 2015 MODIS Mosaic of Greenland [65] (red zoom box; Fig. 1). Zoom box over Midgard, Helheim, Ikertivaq, and Køge Bugt glaciers (red box; Fig. 8). (b) 2015–2019 ice slab (cyan shading), perennial firn aquifer (blue shading), and percolation facies (purple shading) spatial extents mapped using the SMAP rSIR T_V^B image time series [63] and the empirical algorithm [16]. (c) Estimates of snow accumulation (rainbow logarithmic colorscale) simulated via RACMOp2.3 [18]. 18
- 7 2015–2019 scatterplot of the firn saturation parameter values over and ice slab (cyan circles) and perennial firn aquifer (blue circles) grid cells mapped using the SMAP rSIR T_V^B image time series [63] and the empirical algorithm [16] versus snow accumulation grid cells simulated via RACMOp2.3 [18]. 19
- 8 2015–2019 firn saturation parameter spatial extent (semi-transparent rainbow colorscale) and contour intervals (white lines) mapped using the SMAP rSIR T_V^B image time series [63] and the two-layer L-band brightness temperature model [16]; 2017 CReSIS Accumulation Radar (AR) southeastern (red line, transect C-D; Fig. 9d) profile, all overlaid on the 2009–2010 winter season Advanced Land Observing Satellite Phased Array L-band Synthetic Aperture Radar (ALOS-PALSAR) radar backscatter mosaic over Midgard, Helheim, Ikertivaq, and Køge Bugt glaciers [66], [67] (red zoom box; Fig. 6). 20
- 9 (a, c) 2015–2019 firn saturation parameter values mapped using the SMAP rSIR T_V^B image time series [63] and the two-layer L-band brightness temperature model [16] over (b, d) CReSIS Accumulation Radar (AR) southwestern profile collected on 5 May 2017 (orange line, transect A-B; Fig. 5), and southeastern profile collected on 22 April 2017 (red line, transect C-D; Fig. 6). (e) Calculated surface elevation profiles [19]. 21

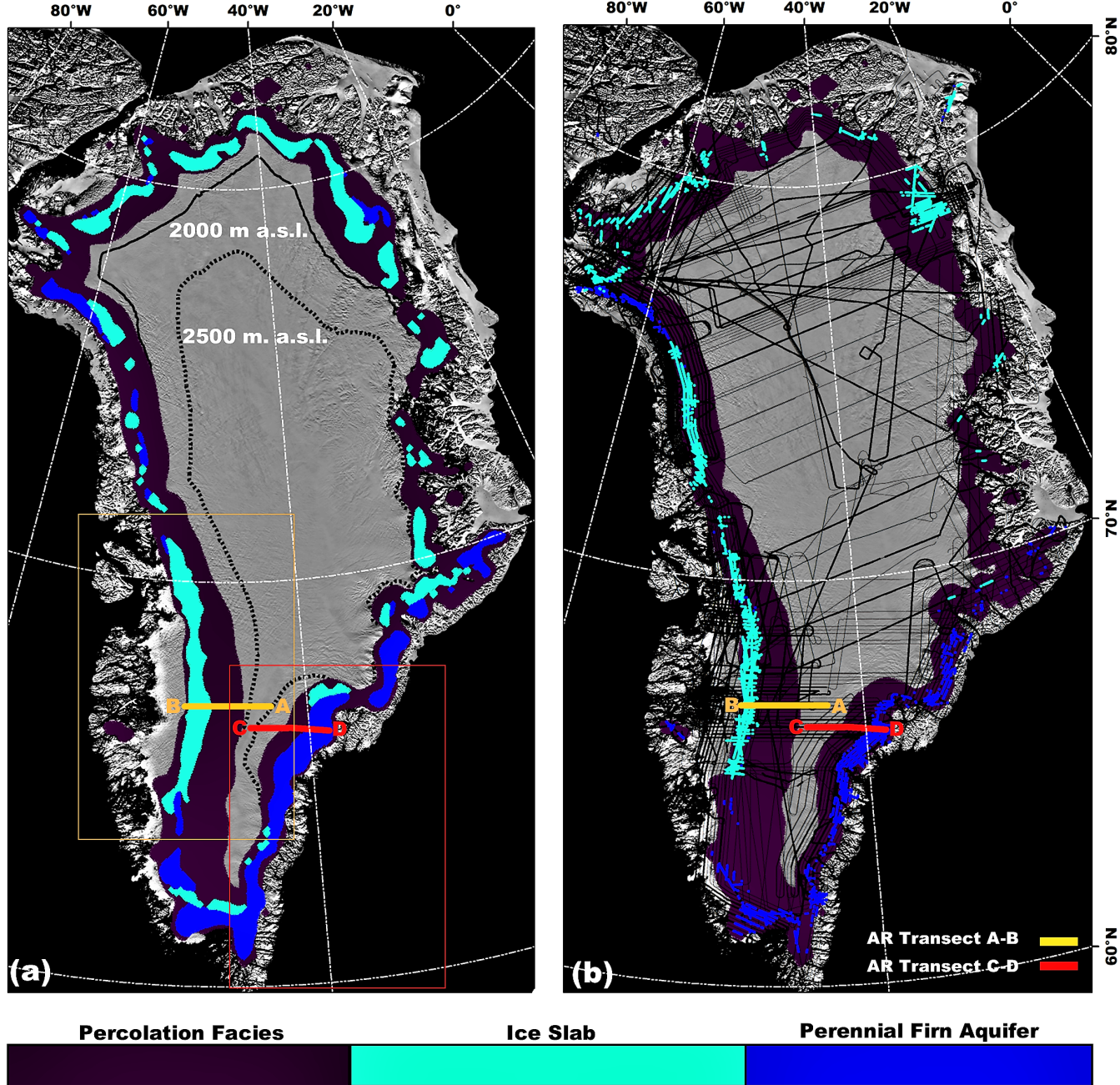


Fig. 1. (a) 2015–2019 ice slab (cyan shading), perennial firn aquifer (blue shading), and percolation facies (purple shading) spatial extents mapped using the SMAP rSIR T_V^B image time series [63] and the empirical algorithm [16]; 2000 m a.s.l. contour (black line) and 2500 m a.s.l. contour (black dotted line) [43], [64]; 2017 CReSIS Accumulation Radar (AR) southwestern (orange line, transect A-B; Fig. 9b) and southeastern (red line, transect C-D; Fig. 9d) profiles, all overlaid on the 2015 MODIS Mosaic of Greenland [65]. Zoom boxes over southwestern (orange box; Fig. 2a-b) and southeastern (red box; Fig. 2c-d) Greenland. (b) CReSIS AR- and MCoRDS-derived 2010–2014 ice slab (cyan shading) [26] and 2010–2017 perennial firn aquifer (blue shading) [32] detections along NASA OIB flight lines (black interior lines).

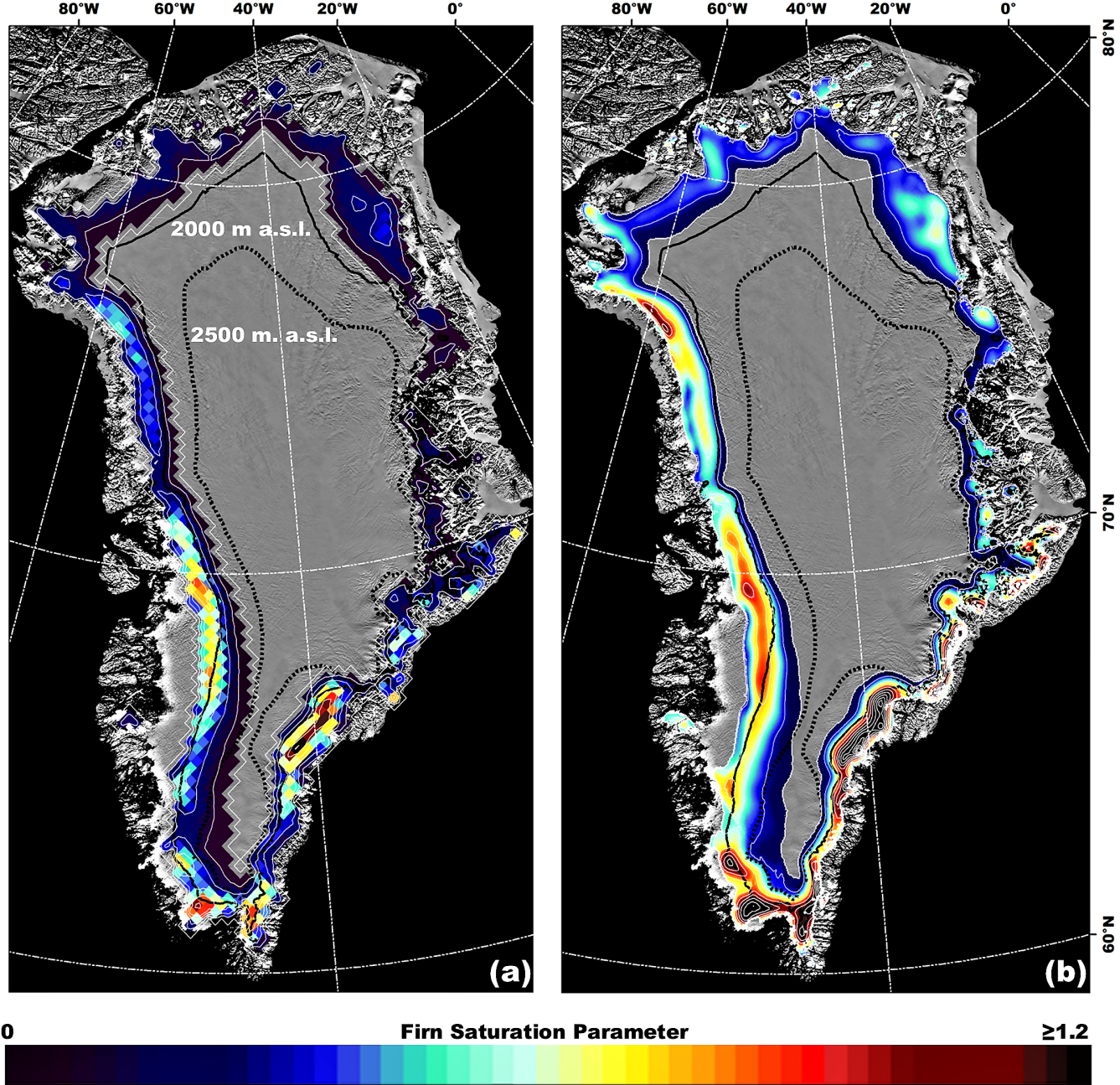


Fig. 2. 2015–2019 firm saturation parameter spatial extent (rainbow colorscale) and contour intervals (white lines) mapped using the SMAP (a) GRD and (b) rSIR T_V^B image time series [63] and the two-layer L-band brightness temperature model [16] overlaid on the 2015 MODIS Mosaic of Greenland [65].

FIGURES

15

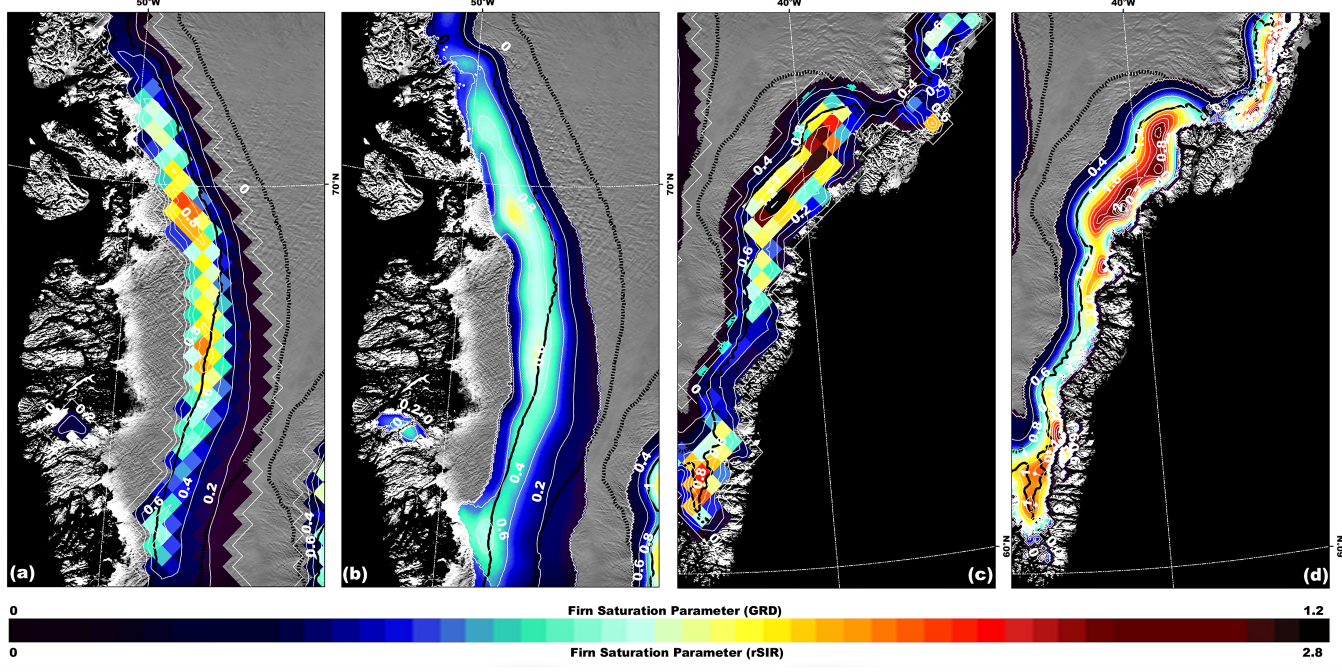


Fig. 3. 2015–2019 firm saturation parameter spatial extent (rainbow colorscale) and contour intervals (white lines) mapped using the SMAP (a-b) GRD and (c-d) rSIR T_V^B image time series [63] and the two-layer L-band brightness temperature model [16] overlaid on the 2015 MODIS Mosaic of Greenland (zoom boxes in Fig. 1a) [65].

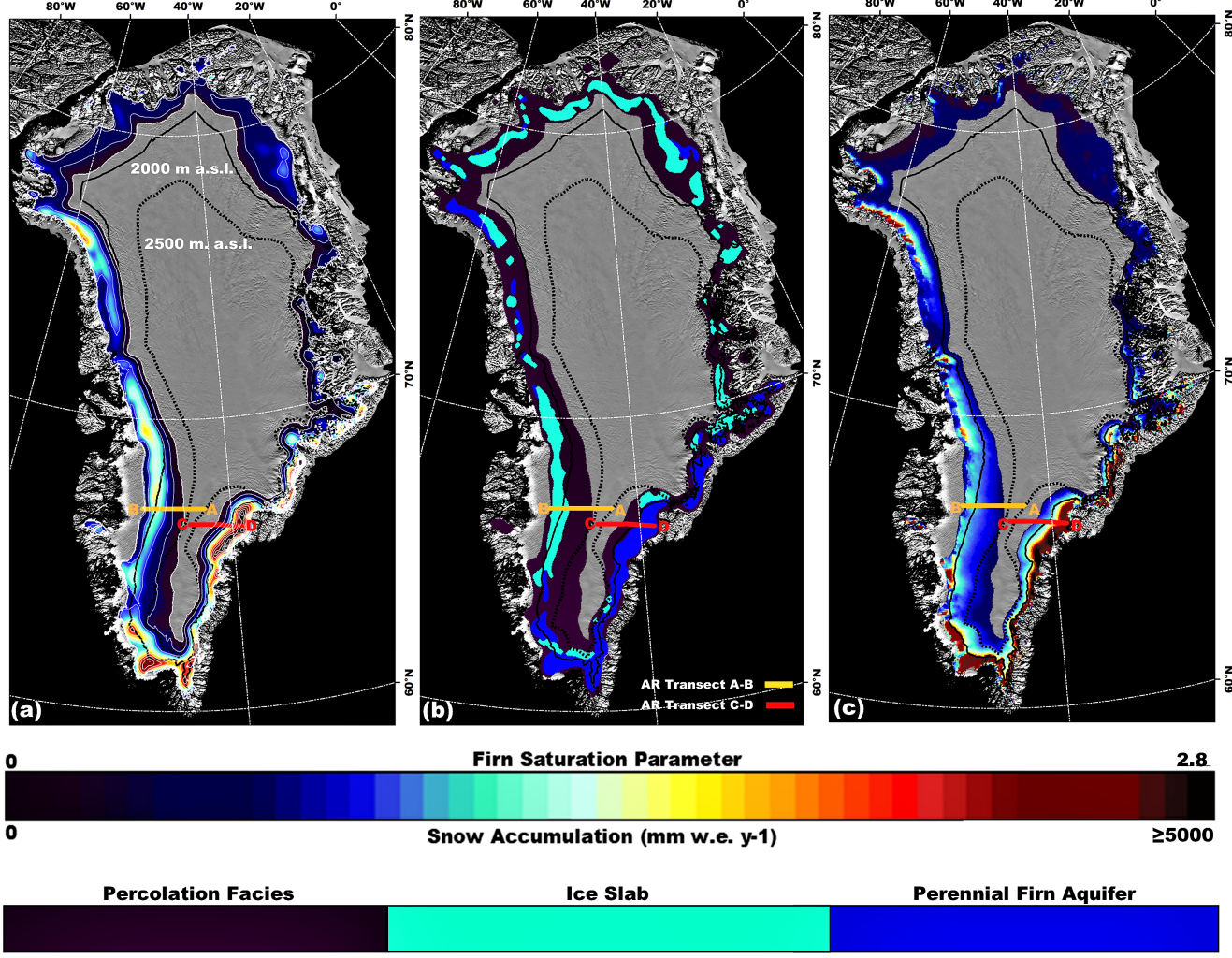


Fig. 4. (a) 2015–2019 firn saturation parameter spatial extent (rainbow colorscale) and contour intervals (white lines) mapped using the SMAP rSIR T_V^B image time series [63] and the two-layer L-band brightness temperature model [16]; 2000 m a.s.l. contour (black line), and the 2500 m a.s.l. contour (black dotted line) [43], [64]; 2017 CReSIS Accumulation Radar (AR) southwestern (orange line, transect A-B; Fig. 9b) and southeastern (red line, transect C-D; Fig. 9d) profiles, all overlaid on the 2015 MODIS Mosaic of Greenland [65]. (b) 2015–2019 ice slab (cyan shading), perennials firn aquifer (blue shading), and percolation facies (purple shading) spatial extents mapped using the SMAP rSIR T_V^B image time series [63] and the empirical algorithm [16]. (c) Estimates of snow accumulation (rainbow logarithmic colorscale) simulated via RACMOp2.3 [18].

FIGURES

17

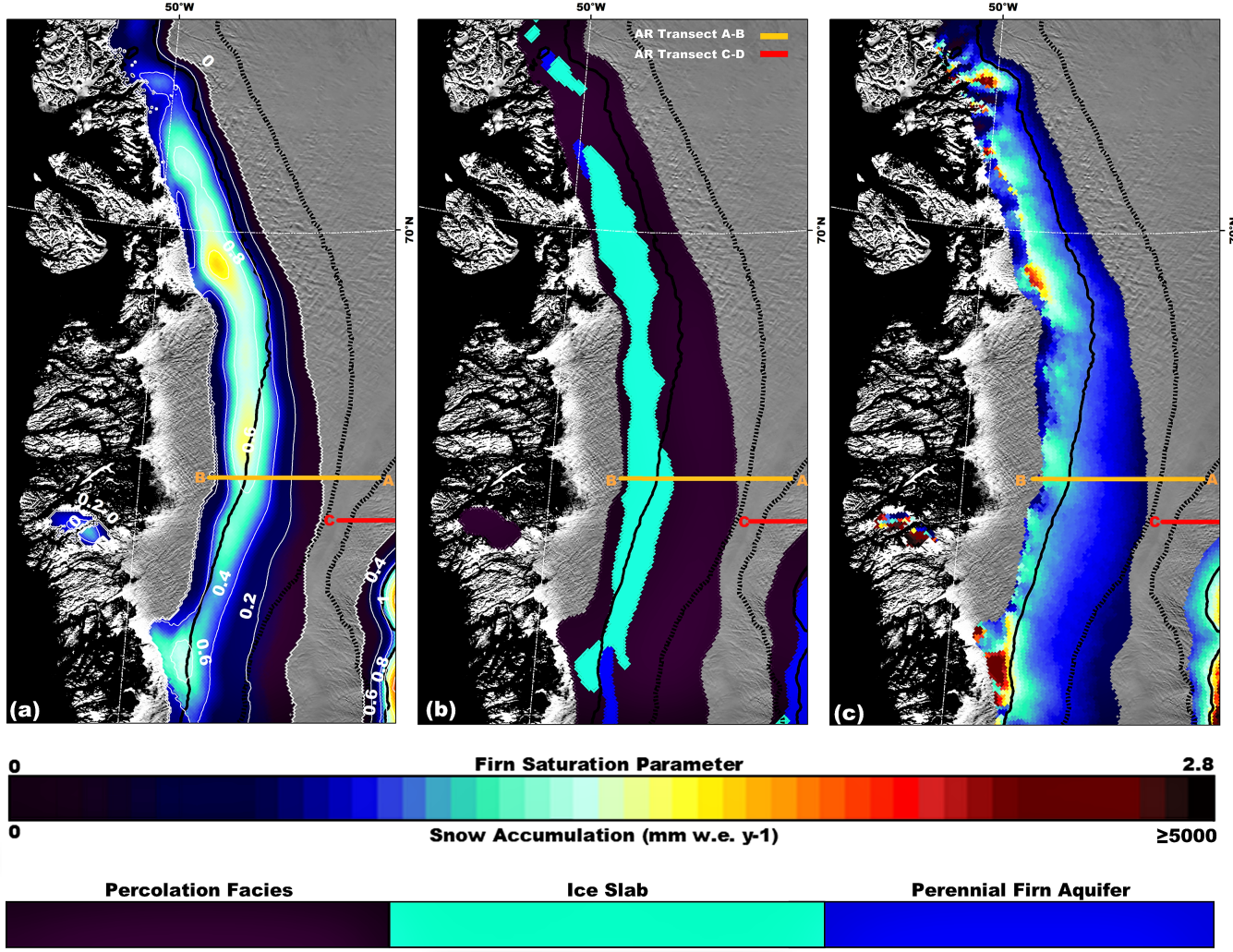


Fig. 5. (a) 2015–2019 firn saturation parameter spatial extent (rainbow colorscale) and contour intervals (white lines) mapped using the SMAP rSIR T_V^B image time series [63] and the two-layer L-band brightness temperature model [16]; 2000 m a.s.l. contour (black line), and the 2500 m a.s.l. contour (black dotted line) [43], [64]; 2017 CReSIS Accumulation Radar (AR) southwestern (orange line, transect A-B; Fig. 9b) profiles, all overlaid on the 2015 MODIS Mosaic of Greenland [65] (orange zoom box; Fig. 1). (b) 2015–2019 ice slab (cyan shading), perennial firm aquifer (blue shading), and percolation facies (purple shading) spatial extents mapped using the SMAP rSIR T_V^B image time series [63] and the empirical algorithm [16]. (c) Estimates of snow accumulation (rainbow logarithmic colorscale) simulated via RACMOp2.3 [18].

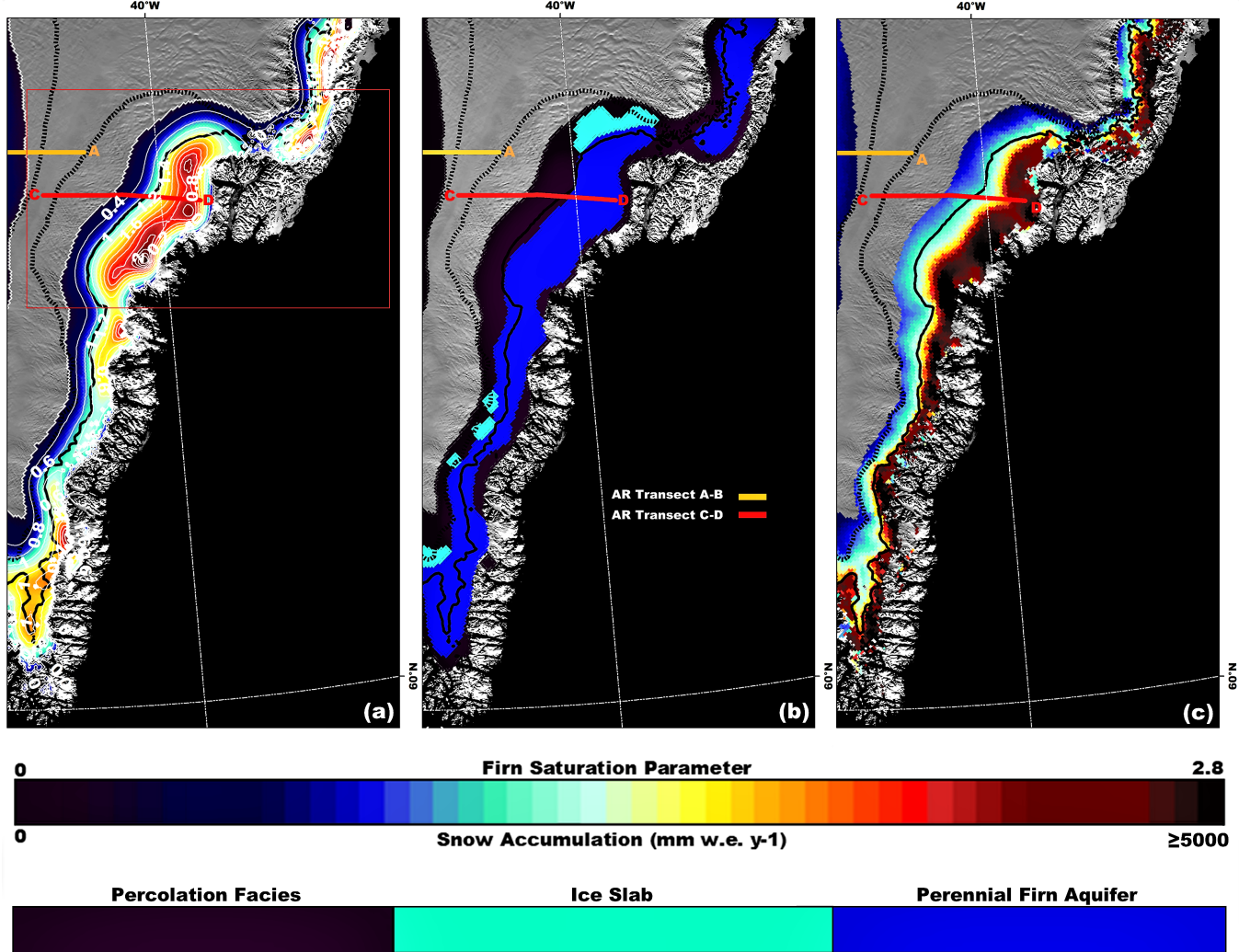


Fig. 6. (a) 2015–2019 firn saturation parameter spatial extent (rainbow colorscale) and contour intervals (white lines) mapped using the SMAP rSIR T_V^B image time series [63] and the two-layer L-band brightness temperature model [16]; 2000 m a.s.l. contour (black line), and the 2500 m a.s.l. contour (black dotted line) [43], [64]; 2017 CReSIS Accumulation Radar (AR) southeastern (red line, transect C-D; Fig. 9d) profile, all overlaid on the 2015 MODIS Mosaic of Greenland [65] (red zoom box; Fig. 1). Zoom box over Midgard, Helheim, Ikertivaq, and Køge Bugt glaciers (red box; Fig. 8). (b) 2015–2019 ice slab (cyan shading), perennial firm aquifer (blue shading), and percolation facies (purple shading) spatial extents mapped using the SMAP rSIR T_V^B image time series [63] and the empirical algorithm [16]. (c) Estimates of snow accumulation (rainbow logarithmic colorscale) simulated via RACMO2.3 [18].

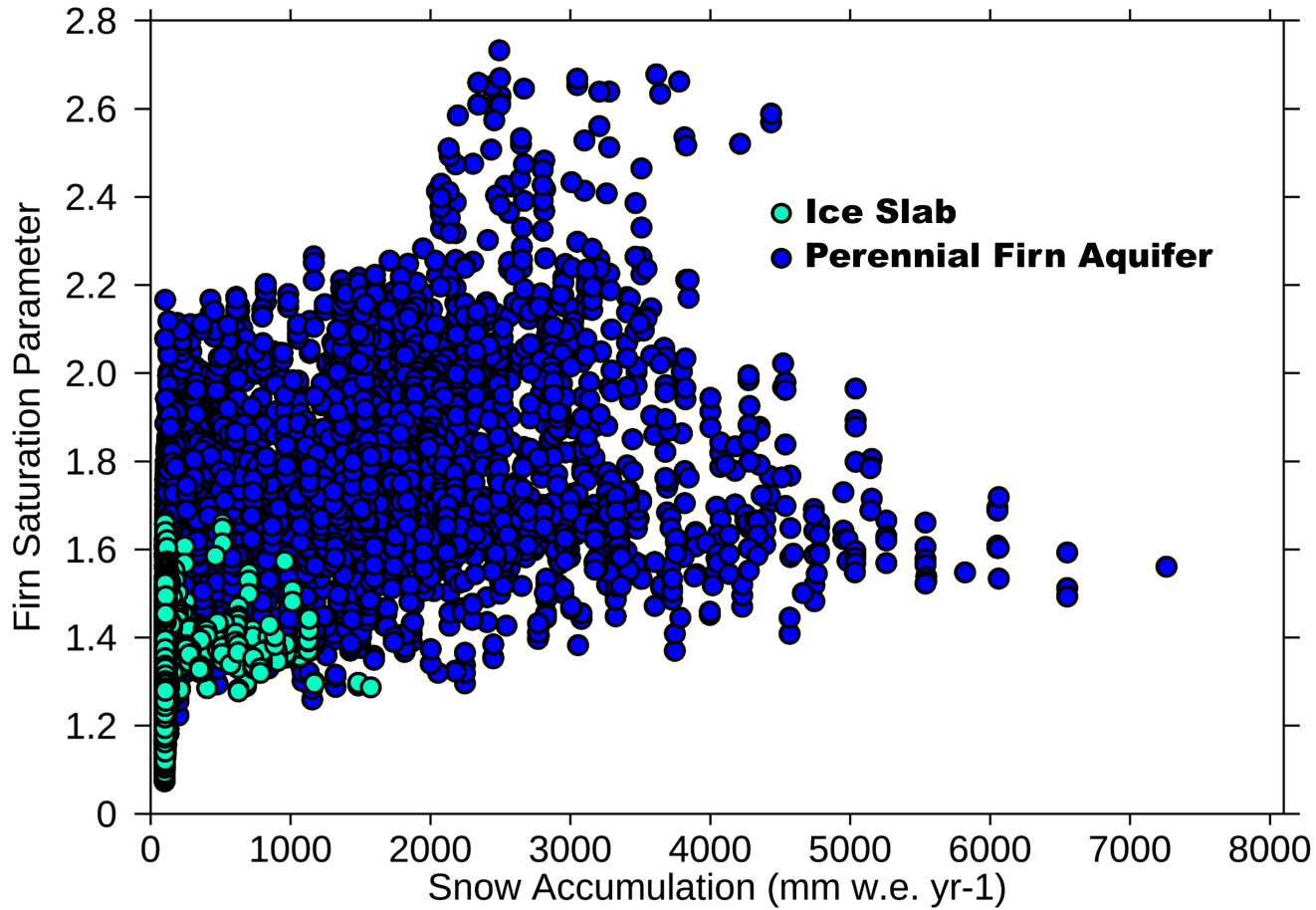


Fig. 7. 2015–2019 scatterplot of the firn saturation parameter values over and ice slab (cyan circles) and perennial firn aquifer (blue circles) grid cells mapped using the SMAP rSIR T_V^B image time series [63] and the empirical algorithm [16] versus snow accumulation grid cells simulated via RACMOp2.3 [18].

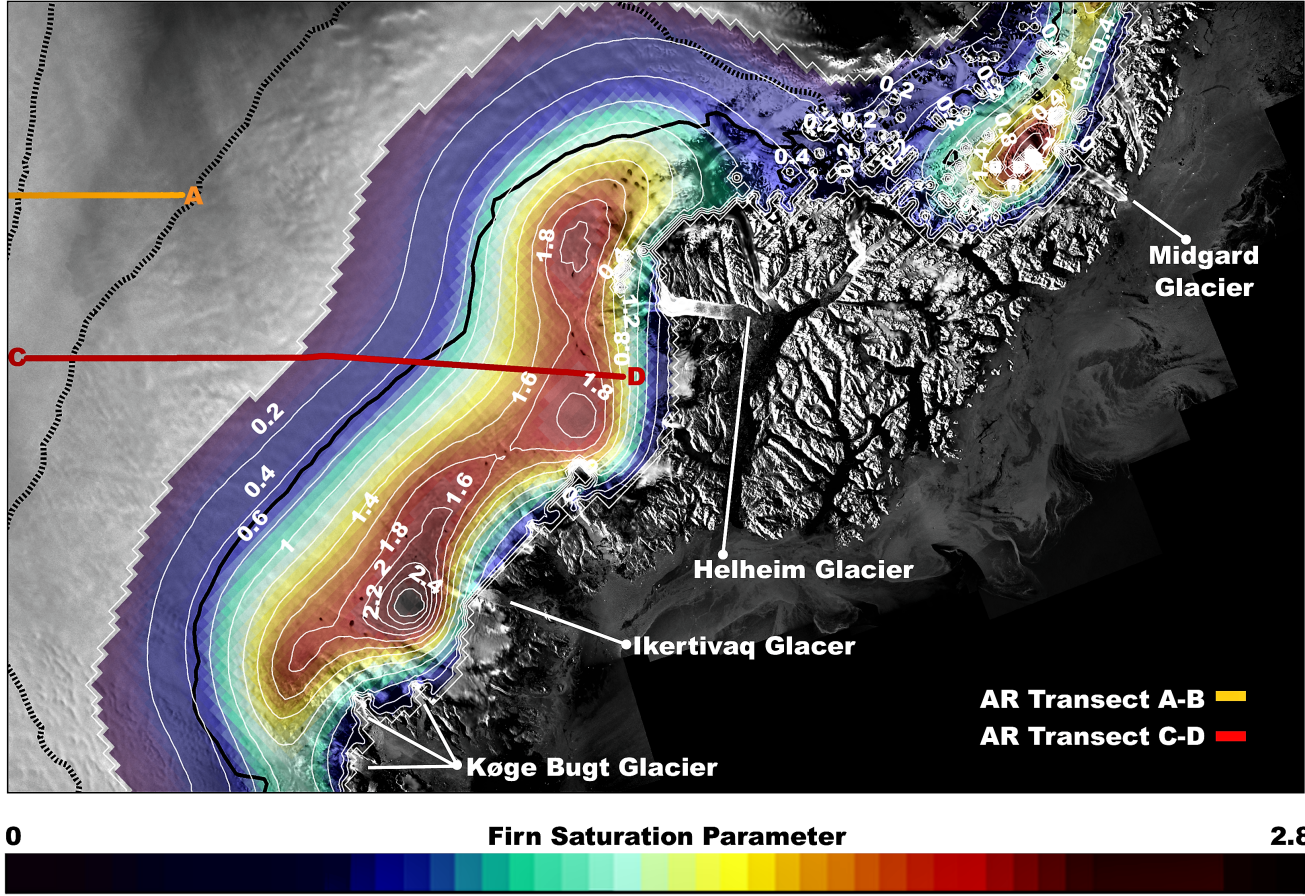


Fig. 8. 2015–2019 firn saturation parameter spatial extent (semi-transparent rainbow colorscale) and contour intervals (white lines) mapped using the SMAP rSIR T_V^B image time series [63] and the two-layer L-band brightness temperature model [16]; 2017 CReSIS Accumulation Radar (AR) southeastern (red line, transect C-D; Fig. 9d) profile, all overlaid on the 2009–2010 winter season Advanced Land Observing Satellite Phased Array L-band Synthetic Aperture Radar (ALOS-PALSAR) radar backscatter mosaic over Midgard, Helheim, Ikertivaq, and Køge Bugt glaciers [66], [67] (red zoom box; Fig. 6).

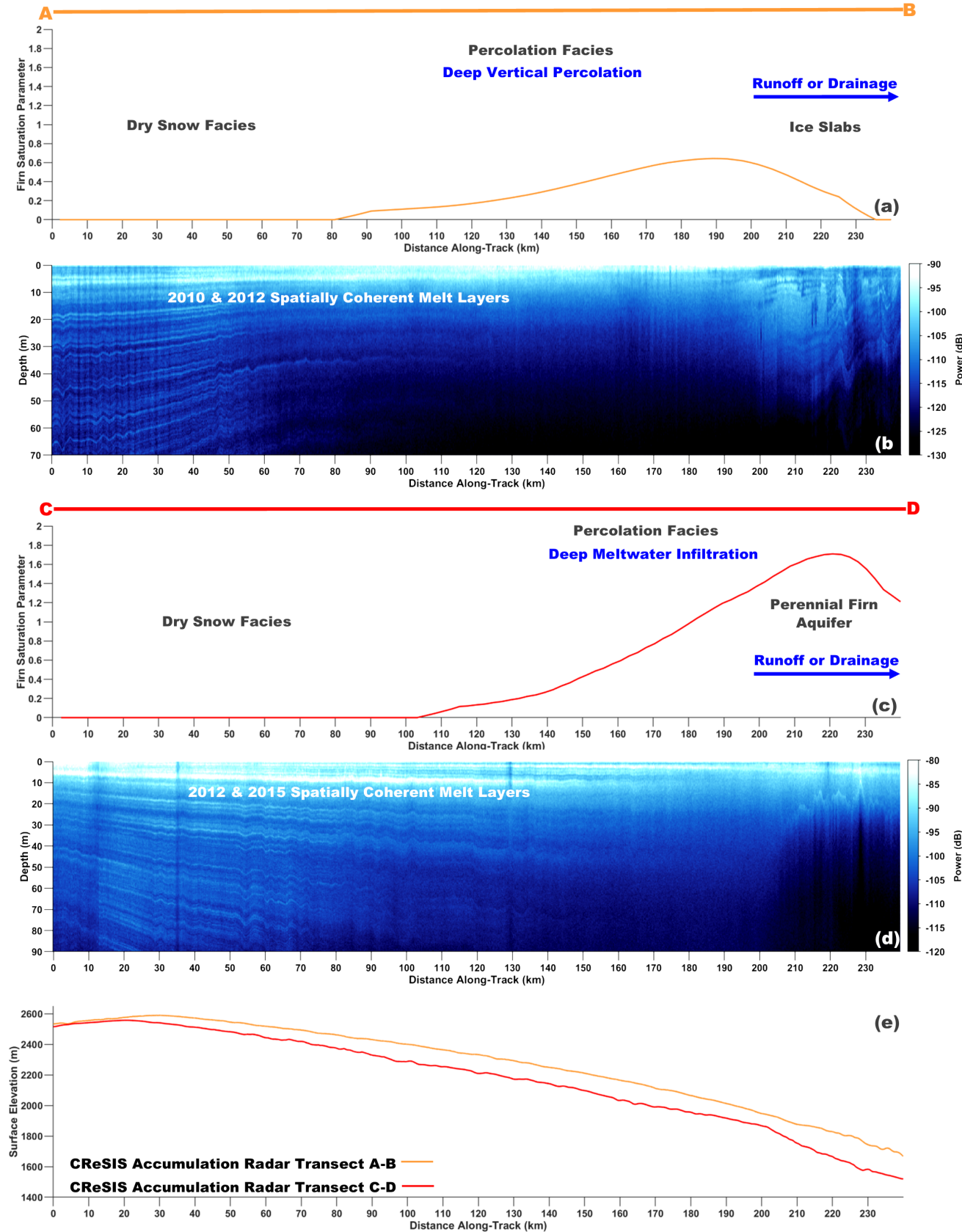


Fig. 9. (a, c) 2015–2019 firn saturation parameter values mapped using the SMAP rSIR T_V^B image time series [63] and the two-layer L-band brightness temperature model [16] over (b, d) CReSIS Accumulation Radar (AR) southwestern profile collected on 5 May 2017 (orange line, transect A-B; Fig. 5), and southeastern profile collected on 22 April 2017 (red line, transect C-D; Fig. 6). (e) Calculated surface elevation profiles [19].

LIST OF TABLES

I	Calibration parameter intervals used in the empirical algorithm.	23
---	--	----

TABLE I
CALIBRATION PARAMETER INTERVALS USED IN THE EMPIRICAL ALGORITHM.

	$T_{V,min}^B$ (K)	$T_{V,max}^B$ (K)	ξ	ζ
Ice Slabs	130 – 240	170 – 260	0.1 – 2.0	-0.06 – -0.03
Perennial Firn Aquifers	180 – 250	200 – 275	0.2 – 2.8	-0.04 – -0.02